Chemical Engineering Science 285 (2024) 119430

Contents lists available at ScienceDirect

Chemical Engineering Science

journal homepage: www.elsevier.com/locate/ces

Mass transfer in atmospheric water harvesting systems

Thomas Lassitter [a], Nikita Hanikel [b], Dennis J. Coyle [c], Mohammad I. Hossain [a], Bryce Lipinski [c], Michael O'Brien [c], David B. Hall [c], Jon Hastings [a], Juan Borja [c], Travis O'Neil [c], S. Ephraim Neumann [b], David R. Moore [c], Omar M. Yaghi [b], T. Grant Glover [a,*]

[a] Department of Chemical & Biomolecular Engineering, University of South Alabama, Mobile, AL 36688, United States
[b] Department of Chemistry and Kavli Energy Nanoscience Institute, University of California, Berkeley, CA 94720, United States
[c] GE Global Research, 1 Research Circle, Niskayuna, NY 12309, United States

A B S T R A C T

In this work, the rate-limiting diffusion mechanisms of MOF-303, MOF-333, and a multivariate (MTV) version of these metal–organic frameworks (MOFs), where the organic linkers are present in a 50/50 ratio, are identified and quantified using concentration swing frequency response (CSFR). The data show that the single-atom precision of MOFs allows for precise tuning of the diffusion rate that is not easily achieved in traditional adsorbent materials. The Maxwell-Stefan diffusivity as a function of loading was calculated to decouple the influence of molecular mobility and equilibrium effects. To further understand the diffusion process in these MOFs, samples with different crystal sizes were synthesized and diffusion rates were measured. The results show that the controlling diffusion length scale is similar between the small and large crystal samples, as evidenced by similar diffusion rate constants. The MOFs were then incorporated into a film using a binder system and the mass transfer mechanisms were identified using CSFR. When placed in this particular binder system, the macropore diffusion behavior dominates over the MOF micropore diffusion. To illustrate how these diffusion parameters govern the adsorption rates and dynamics of water-harvesting systems, a model of the MOF-coated tube was developed. The results show that, with only milligrams of adsorbent, CSFR can quantify the diffusion rate needed to predict the adsorption times in a water-harvesting system. More broadly, the results illustrate the connectivity between atomically-precise reticular chemistry and water-harvesting system performance.

1. Introduction

A variety of technologies exists to purify water including desalination, distillation, filtration, and reverse osmosis. However, these techniques each depend on access to a liquid water source, which may not always be available. To address this issue, atmospheric water harvesting (AWH) technology has been developed, which provides an alternative to locating, cleaning, and moving liquid water to its end application location. (Tu et al., 2018; Yang et al., 2021; Alsaedi, 2018; Bagheri, 2018; Fathieh et al., 2018; Kalmutzki et al., 2018; Macedonio et al., 2012; Zhou et al., 2020; Kim et al., 2017; Kim et al., 2018; Hanikel et al., 2019).

Several methods exist to collect water from the atmosphere including dehumidifying devices based on refrigerants as well as dew and fog collection systems. However, refrigerant-based systems are limited to dew points near 0–5 °C, and dew/fog collection systems are limited to geographic regions where dew and fog are present. Adsorbent-based materials do not suffer from these limitations and provide a means of collecting water in exceptionally dry environments. (Klemm et al., 2012; Gido et al., 2016; Peeters et al., 2020).

While a wide variety of adsorbent materials exists that can capture water, careful selection of a material to provide a practical and energetically efficient system requires an understanding of the water working capacity of the material, the energy required to release the adsorbed water, and the ease with which the material can be implemented into a mechanical system. (Yang et al., 2021; Zhou et al., 2020) For example, traditional porous adsorbent materials, such as zeolites 13X and 5A, have a steep adsorption isotherm at low RH resulting in a high water loading, but the water is adsorbed very strongly, which increases the energy requirements for regeneration and makes these adsorbents less practical for water harvesting. (Kalmutzki et al., 2018; Zhou et al., 2020; LaPotin et al., 2020) Likewise, silica gels (Sleiti et al., 2021) adsorb water less strongly than zeolites but have an almost linear adsorption isotherm with some hysteresis, which may diminish the working capacity of the material. (Kalmutzki et al., 2018; Zhou et al., 2020; Rajniak and Yang, 1993) Activated carbon on the other hand adsorbs a significant amount of water and has an "S-shaped" adsorption isotherm, which is important when considering the working capacity during adsorption cycling, but the majority of the water loading occurs at 40 % relative humidity (RH) or higher over the temperature range of 25–125 °C, limiting its relevance as a water-harvesting material. Also, similar to silica gel, the water adsorption isotherm of activated carbon contains

* Corresponding author.
E-mail address: glover@southalabama.edu (T. Grant Glover).

https://doi.org/10.1016/j.ces.2023.119430
Received 10 May 2023; Accepted 23 October 2023
Available online 9 November 2023

some hysteresis. (Rudisill et al., 1992).

Salts are also commonly examined as candidate materials because of their low cost and wide availability. However, the performance of salts can be limited due to deliquescence, which hinders kinetics, leads to system corrosion, and may result in challenges with the recovery of the solid sorbent. (Yang et al., 2021; Zhou et al., 2020; Li et al., 2018) To solve this problem, salts are often incorporated into porous materials, (Xu et al., 2020; Ji et al., 2007; Kallenberger and Fröba, 2018) hollow structures, (Li et al., 2020; Yang et al., 2020) or polymer networks. (Li et al., 2018; Yang et al., 2021) However, because the mechanism of water capture is still driven by the salt in the pore, these composite materials must still contend with deliquescence in the pores, poor adsorption kinetics, and challenging regeneration requirements. (Zhou et al., 2020) Additionally, salts contained in porous materials may change over time and age with repeated adsorption and desorption cycles. (Rossin et al., 1991) Likewise, liquid sorbents, such as concentrated salt solutions, (Wang et al., 2019) also have high uptake capacity, but suffer from kinetic limitations and high energy requirements for desorption relative to other adsorbents. (Yang et al., 2021; Zhou et al., 2020).

With these design constraints in mind, MOFs are appealing for water harvesting because these materials can provide single-atom scale control of the water adsorption isotherm. (Glover and Mu, 2018; Yaghi et al., 2019) In this way, MOFs can be designed for water adsorption in a specific RH range via an S-shaped isotherm and the hysteresis commonly seen in other adsorbents is not as prevalent. The control of the S-shaped adsorption portion of the isotherms, coupled with limited hysteresis, results in a large working capacity, which facilitates system design by enabling the almost stepwise release of water during desorption. (Kalmutzki et al., 2018; Roque-Malherbe, 2007) These key features position MOFs as the optimal adsorbents for water sorption applications in any climate. (Kalmutzki et al., 2018; Hanikel et al., 2019; Xu and Yaghi, 2020; Rieth et al., 2019; Towsif Abtab et al., 2018; Logan et al., 2020).

While numerous materials have been examined for water harvesting from a thermodynamic capacity perspective, less effort has been devoted to understanding the kinetics of gas adsorption. But the kinetics of the adsorption process are equally important, especially when the adsorbent is actively cycled between adsorption and desorption to increase water yield. In general, there is a lack of available data detailing the transport diffusion of water vapor in MOFs, which limits the design of water-harvesting systems and more broadly the understanding of mass transfer in porous materials. (Hossain and Glover, 2019; Laurenz et al., 2021; Canivet et al., 2014; Canivet et al., 2014; Burtch et al., 2014; Nemiwal and Kumar, 2020; Furukawa et al., 2014).

Diffusion in adsorbents is complex and requires an explanation to describe the different diffusion parameters that are reported in the literature. (Skoulidas and Sholl, 2005) Skoulidas *et al.*, provide an explanation of diffusion detailing that Eq. (1) describes the transport diffusion where D_t is the transport diffusivity that is the proportionality constant relating macroscopic flux to a spatial concentration gradient in Fick's law. The transport diffusivity is also commonly referred to as either the Fickian diffusivity, the chemical diffusivity, or the collective diffusivity. However, it is often convenient to define the transport diffusivity in terms of the corrected diffusivity D_0 as shown in Eq. (2). The partial derivative involving concentration and fugacity is the thermodynamic correction factor and is defined by the single-component adsorption isotherm. The corrected diffusivity is equal to the Maxwell-Stefan diffusivity in single-component systems.

It is important to distinguish the transport diffusivity from the self-diffusivity, D_{sf}, as the self-diffusivity describes the motion of individual particles at an equilibrium condition versus the movement of molecules under a concentration gradient. In an isotropic, three-dimensional material, the self-diffusivity is related to the mean-squared displacement of tagged particles after time t by the Einstein relation as shown in Eq. (3), where $\vec{\mathbf{r}}(t)$ is the position vector of a tagged particle at time t and the angular brackets indicate an ensemble average. (Skoulidas and Sholl, 2005) In dilute concentrations, the diffusivities are equal. In applications where it is necessary to describe net mass transfer under non-equilibrium conditions, such as modeling membranes or pressure-swing adsorption systems, it is the transport diffusivity that is of particular interest. (Skoulidas and Sholl, 2005)

$$J = -D_t(c)\nabla c \tag{1}$$

$$D_t(c) = -D_0(c)\left(\frac{\partial \ln f}{\partial \ln c}\right)_T \tag{2}$$

$$D_{sf}(c) = \lim_{t\to\infty}\frac{1}{6t}\left\langle \left| \vec{\mathbf{r}}(t) - \vec{\mathbf{r}}(0) \right|^2 \right\rangle \tag{3}$$

There are several techniques available to measure the diffusion of gases in MOFs which can be broadly divided into macroscopic methods, including gravimetric and volumetric uptake methods, zero-length column (ZLC) chromatography, (Brandani et al., 1996; Brandani et al., 1995; Eic and Ruthven, 1989; Gunadi and Brandani, 2006; Silva and C., Rodrigues, A. E., 1996) and frequency response (FR), which measure transport diffusivity; and microscopic methods, which includes quasi-elastic neutron scattering (QENS), pulsed field gradient (PFG) nuclear magnetic resonance (NMR), and infrared (IR) spectroscopy, which measure self-diffusivity. (Glover and Mu, 2018; Sharp et al., 2021) While some microscopic methods can measure transport diffusivities, such as coherent QENS and IR spectroscopy, (Sharp et al., 2021) they typically measure self-diffusivities.

Of these methods, FR techniques can identify and quantify the rate-limiting mass transfer mechanism. (Glover and Mu, 2018; Wang, 2021; Wang and LeVan, 2011) In particular, frequency response is a technique whereby one variable of a system in equilibrium is perturbed periodically and the response of another variable is monitored. Because the technique is periodic, there is less dependence on the initial conditions of the system and random error tends to average out over many oscillatory periods, which is another advantage of this method. Further, to generate one data set, the experiment is repeated over a broad range of perturbation frequencies reducing error that might be associated with calculating the diffusion rate based on one experimental data set.

Although numerous models could be examined with FR, the models shown in Eqs. (4)–(6) are helpful when considering diffusion in solid-phase adsorbents.

$$\text{External Fluid Resistance } \rho_b\frac{dn}{dt} = k_f a\left(c - c_s^*\right) \tag{4}$$

$$\text{Micropore Diffusion } \frac{\partial n}{\partial t} = \frac{D_s}{r^2}\frac{\partial}{\partial r}\left(r^2\frac{\partial n}{\partial r}\right) \tag{5}$$

$$\frac{\partial n}{\partial t} = 0 \ at \ r = 0$$

$$n = n^* \ at \ r = R$$

$$\text{Linear Driving Force } \frac{dn}{dt} = k_n(n^* - n) \tag{6}$$

In particular, Eq. (4) describes the transport of molecules to the surface of the adsorbent driven by the difference in concentration in the fluid phase, where c is the fluid phase concentration, c_s^* is the concentration in the fluid at the adsorbent particle, ρ_b is the density, a is the area, t is time, and k_f is the transport coefficient. Molecules on the surface of the adsorbent then diffuse into the particle and the diffusion can be described by different models (Eqs. (5)–(7)) depending on the governing mechanism.

Eq. (5) provides a model where surface diffusion is governing based on a description of the microparticle as spherical in the nanoporous domain where n is the adsorbate concentration in the nanopore, n^* is the equilibrium adsorbate concentration in the equilibrium state, r is the

radial coordinate for the microparticle (i.e., nanoporous domain), R is the radius of the microparticle, and D_s is the diffusivity.

However, a linear driving force can also be used to describe the diffusion into the adsorbent, as shown in Eq. (6) where k_n is the linear driving force coefficient. (Glueckauf, 1955; Hossain et al., 2016; Do and Mayfield, 1987) The linear driving force model can provide an accurate approximation of diffusion; however, it is also useful for describing systems in which the rate-limiting mass transfer step is a surface barrier where a constriction at the pore mouth is the dominant resistance, as discussed by Wang and Levan. (Wang and LeVan, 2011).

For some adsorbents, resistance in the macropore must also be accounted for and can be described as

$$\rho_p \frac{\partial n}{\partial t} + \varepsilon_p \frac{\partial c_p}{\partial t} = \frac{\varepsilon_p D_p}{r^2} \frac{\partial}{\partial r}\left(r^2 \frac{\partial c_p}{\partial r}\right) \tag{7}$$

$$c_p = c \ at \ r = R_p$$

$$\frac{\partial c_p}{\partial r} = 0 \ at \ r = 0$$

where ρ_p is the particle density, ε_p is the macroporosity, c_p is the gas-phase concentration in the macropores, r is the radial coordinate, and R_p is the radius of the macropore domain. For a linearized system, the adsorbed phase concentration is in equilibrium with the gas phase concentration in the macropores such that

$$n^* = Kc_p \tag{8}$$

where K is the isotherm slope. With the linearized isotherm, Eq. (7) can be simplified as,

$$\frac{\partial c_p}{\partial t} = \frac{1}{\left(1 + \frac{\rho_p K}{\varepsilon_p}\right)} \frac{D_p}{r^2} \frac{\partial}{\partial r}\left(r^2 \frac{\partial c_p}{\partial r}\right) \tag{9}$$

where Eq. (9) has the same mathematical form as Eq. (5)(Ruthven, 1984) even though the type of concentration being described, and the type of diffusivity are different. Thus, the analytical solution of micropore diffusion and macropore diffusion model will be the same, and any data set that can be fit by the micropore diffusion model will be fit equally well by the macropore diffusion model. The fitting parameter for these models can be defined as η where this term corresponds to macropore or micropore depending on the governing phenomena as (Tovar et al., 2016; Tovar, 2016)

$$\frac{D_s}{r^2} \xleftarrow{micropore} \eta \xrightarrow{macropore} \frac{\frac{D_p}{r^2}}{\left(1 + \frac{\rho_p K}{\varepsilon_p}\right)} \tag{10}$$

Thus, fitting data to these models alone cannot identify micropore versus macropore mass transfer control. However, the characteristic length for macropore diffusion is the effective radius of the particle, whereas for micropore it is a smaller micropore radius. Thus, if the mass transfer is controlled by the macropore diffusion the mass transfer parameter will be a function of the particle size of the adsorbent, whereas if micropore diffusion is the controlling mechanism, the mass transfer parameter will not be strongly dependent on particle size. This approach allows for the differentiation of the mechanism, which is important as the macropore model has been found to be the governing resistance in some adsorbents (Giesy and LeVan, 2013; Hossain et al., 2019; Tovar, 2016).

Lastly, transport diffusivities depend on the adsorbed phase loading, and in systems with sharp changes in adsorption loading as a function of pressure, such as those in water-harvesting MOFs, it is helpful to separate the influence of a steep adsorption isotherm on the measured kinetic rate. This can be accomplished following the approach outlined by Ruthven (Ruthven, 1984) where Eq (1) is written in terms of the gradient in chemical potential to produce the Maxwell-Stefan form of the flux equation,

$$J_i = -Bc \frac{\partial \mu}{\partial x} \tag{11}$$

$$\mu = \mu_o + RT \ln p \tag{12}$$

$$\frac{\partial \mu}{\partial x} = RT \frac{d \ln p}{dc} \frac{\partial c}{\partial x} \tag{13}$$

$$J = -BRT \frac{d \ln p}{d \ln c} \frac{\partial c}{\partial x} \tag{14}$$

$$D_t = BRT \frac{d \ln p}{d \ln c} = D_0 \Gamma \tag{15}$$

where B is the molecular mobility, c is the total concentration in the pore, and $\frac{\partial \mu}{\partial x}$ is the gradient in chemical potential, and substitution leads to an expression where BRT is referred to as D_0, the corrected diffusivity. (Ruthven, 2004; Ruthven et al., 2008) This term accounts for the molecular mobility effects. The $\frac{d \ln p}{d \ln c}$ term is referred to as the thermodynamic correction factor, and accounts for the equilibrium effects on the measured diffusivity and can also be written as Γ. Therefore, for a system of interest with an experimentally measured isotherm, it is possible to calculate the thermodynamic correction factor and the value of corrected diffusivity, D_0, can be determined using an experimental value of the diffusivity obtained at a particular pressure.

Procedurally, the ratio of the amplitude of the response to the amplitude of the perturbation is plotted against the perturbation frequency, and a transfer function comprised of the models discussed is used to model the response. Because the shape of the response curve is dictated by the assumed mechanism, only appropriate models will accurately fit the data. The sensitivity of the technique to different models can prevent erroneously assuming a governing mass transfer resistance. Also, the technique helps prevent unknowingly fitting numerous adsorption phenomena, such as heat effects, pressure drop, and dispersion, into a mass transfer term. (Knox et al., 2016; Wang et al., 2021).

FR experiments have utilized perturbations in the volume of a batch system, (Yasuda, 1976; Yasuda, 1982; Yasuda and Matsumoto, 1989; Yasuda, 1993; Hossain et al., 2019; Valyon et al., 2000; Song and Rees, 1997; Song and Rees, 2000; Song and Rees, 2008; Onyestyák et al., 1995; Onyestyák et al., 1996; Onyestyák and Rees, 1999; Hossain et al., 2019; Hossain, 2014) as well as perturbations in the flow rate, (Park et al., 1998; Park et al., 1998) pressure, (Sward and LeVan, 2003; Wang et al., 2003; Wang and LeVan, 2005; Wang and LeVan, 2005; Giesy and LeVan, 2013; Wang and LeVan, 2008) and concentration (Deisler and Wilhelm, 1953; Glover et al., 2008; Hossain and Glover, 2019; Kramers and Alberda, 1953; Li et al., 1989; Liu et al., 2010; Tovar et al., 2016; Wang et al., 2013; Wang and LeVan, 2007; Tovar, 2016) of the inlet of a flow system. Of these methods, flow-through FR methods are advantageous because the flow-through design reduces heat effects thereby allowing the system to be treated isothermally. Additionally, concentration swing frequency response (CSFR) is preferred when only a small amount of adsorbent is available as it can be used to examine single adsorbent particles and crystals. (Glover et al., 2008; Wang and LeVan, 2007) This is especially useful in the characterization of newly designed materials, of which only a small amount may be available.

In this work, CSFR was used to examine the diffusion of water in MOF-303. To illustrate the atomic-scale control that reticular chemistry provides over macroscopic mass transfer properties, MOF-333, which is isostructural to MOF-303 and contains furan-2,4-dicarboxylate in place of 1*H*-pyrazole-3,5-dicarboxylate, was also examined. With these data measured, a diffusion rate between these values was targeted through the synthesis of an MTV variant of MOF-303 and MOF-333, 4/4-MTV-MOF, where the linkers are in a 50/50 ratio. The diffusion rates of

each MOF as a function of concentration and crystal size were determined. Lastly, the mass transfer data were used to model the breakthrough behavior of MOF-303 on both a coated tube and a packed-bed and the relationship between convective flow and solid phase diffusion is considered in the context of atmospheric water harvesting.

2. Experimental

2.1. CSFR system and mathematical models

A CSFR system, similar to the one used by Glover *et al.*, was used to complete the CSFR measurements. (Glover et al., 2008) Helium was passed through a water saturator cell that was located in a temperature-controlled water bath, allowing for gas phase water concentrations to be controlled by setting the water bath temperature. The pressure was controlled at 50 torr above atmospheric pressure using a pressure controller (MKS Baratron type 640B) upstream of the saturator. A second helium stream was mixed with the adsorbate feed stream prior to the adsorbent bed. Both streams were controlled using MKS mass flow controllers and the adsorbate gas concentration fed to the adsorbent bed was determined by the combined flow rates of the two streams. The effluent gas from the adsorbent bed was sampled by an Agilent 5973 mass spectrometer.

Dry weights for the CSFR experiment are required and the amount of sample used for each CSFR experiment is listed in the Supplemental Information (SI). For MOF-303, several grams of material were available and a dry weight was determined by first outgassing 100–200 mg of powder at 120 °C under vacuum using a Micromeritics Smart Vac Prep unit for 12 hrs. The CSFR bed was then loaded with a smaller portion of the dried material. Then the Micromeritics sample cell containing the residual not loaded in the CSFR bed was outgassed and the dry weight of the residual MOF-303 was determined. The weight in the CSFR bed was determined by the difference in the dry weights of the sample contained in the Micrometrics sample cell.

Smaller quantities of MOF-333 and 4/4-MTV-MOF were available compared to MOF-303, and it was not possible to load a sample cell for outgassing without losing the majority of the sample. Therefore, the vial containing the sample was used to determine the weight in a similar approach as was done for MOF-303. In this case, the vial containing the sample and its plastic cap were weighed, the cap was removed, and the sample was baked in an oven at 90 °C for 12 hrs. At the end of 12 hrs, the vial was capped and weighed. The CSFR bed was then loaded, and the vial was baked again without the cap at 90 °C for 12 hrs, at the end of which the vial was capped and the dry weight of the residual was measured. The weight in the CSFR bed was determined by the difference in the dry weight of the sample vial.

Additional material was available when examining larger-crystal versions of MOF-303, 333, and MTV. Therefore, the larger crystal samples (MOF-303, MOF-333, 4/4-MTV-MOF) were regenerated using a TA Q500 Thermogravimetric Analyzer under a dry flow of nitrogen at 15 mL/min and heated to 120 °C with a ramp rate of 2 °C/min and held isothermally at 120 °C for 15 hrs. The CSFR bed was weighed, the sample was loaded after TGA regeneration, and after loading the sample in the CSFR bed, helium was pushed across the bed for 12 hrs. After 12 hrs, the bed was weighed again to determine the dry weight.

After regeneration, the adsorbent was placed in the adsorbent bed at room temperature (25 °C), and a constant, unperturbed feed of water in helium at the selected humidity was passed through the bed overnight to equilibrate the bed at the selected water loading. The flow rates of the two helium streams were perturbed sinusoidally at a selected frequency and each stream was 180 degrees out of phase relative to the other. The resulting feed stream to the adsorbent bed had a constant total flow rate with a sinusoidal adsorbate concentration oscillating around the equilibrium state. To maintain the linearity of the system, the amplitude of the perturbations for both streams was kept small. Specifically, the swing used in this work was ± 0.4 sccm on each stream. In this work, CSFR experiments were conducted over a frequency range of 0.00005 to 0.05 Hz. Unless noted otherwise, all measurements were performed at 25 (±1 °C).

The mathematical model described by Wang and LeVan (Wang and LeVan, 2007), as well as the kinetic rate equations given by Wang *et al.* and Wang and LeVan, were used to model the system. (Wang and LeVan, 2011; Sward and LeVan, 2003; Giesy and LeVan, 2013) For a non-isothermal condition, the particle was assumed to be at a uniform temperature, and the heat transfer resistance was assumed to be between the bed and the bed wall. The energy balance was written as,

$$m_b C_s \frac{\partial T}{\partial t} + m_b \Delta H_a \frac{\partial n}{\partial t} = F_{in}\widehat{h}_{in} - F_{out}\widehat{h}_{out} - hA(T - T_{wall}) \tag{16}$$

where m_b is the mass of adsorbent, C_s is solid heat capacity, T is the temperature, ΔH_a is isosteric heat of adsorption, $\widehat{h}$ is enthalpy,h is the heat transfer coefficient between the bed and the wall, and A is the area of the bed for heat transfer. Since the amplitude of the perturbation in concentration in CSFR experiments was small, the isotherm was linearized as

$$n^* = n_{ref} + K\left(P - P_{ref}\right) \tag{17}$$

where K is the local slope of the isotherm, $\frac{\partial n}{\partial P}$ evaluated at P_{ref}. In the case of non-isothermal conditions, the linearized isotherm can be expressed as,

$$n^* = n_{ref} + K\left(P - P_{ref}\right) - K_T\left(T - T_{ref}\right) \tag{18}$$

where K_T is the negative of the slope of the isobar evaluated at T_{ref}.

2.2. Synthesis of MOFs and production of MOF-coated tube

MOF-303 was synthesized using the procedure outlined in the SI of previous work. (Hanikel et al., 2019) Briefly, 1*H*-pyrazole-3,5-dicarboxylic acid, monohydrate (7.50 g, 43.1 mmol) was dissolved in deionized H_2O (725 mL) and LiOH solution (2.57 M, 25 mL). The resulting solution was heated for 30 min in a preheated oven at 120 °C. Afterward, AlCl3·6H_2O (10.4 g, 43.1 mmol) was added to the solution. Any precipitate was dissolved under sonication and vigorous shaking. Once a clear solution was obtained, the hot reaction mixture was put in a preheated oven at 100 °C, where it was kept for 15 hrs. Then, the precipitate was filtrated out and washed with water. The white solid was subsequently washed with methanol for 24 hrs in a Soxhlet apparatus and air-dried for 3 days. The product was further dried under vacuum ($<10^{-2}$ mbar) for 24 hrs. Full activation of the MOF was conducted under vacuum ($\sim10^{-3}$ mbar) and at 150 °C for 6 hrs, yielding a pure, desolvated product (3.6 g). MOF-333 and 4/4-MTV were synthesized using the procedure outlined in the SI of previous work, (Hanikel et al., 2021) where MOF-333 was composed from the single linker furan-2,4-dicarboxylate, and the 4/4-MTV-MOF exhibited a 1:1 ratio between 1*H*-pyrazole-3,5-dicarboxylate and furan-2,4-dicarboxylate.

For the packed-bed experiments and the experiments involving MOF coated on tube walls, MOF-303 was purchased from NovoMOF and used as received. The MOF-coated tubes containing different thicknesses of MOF coating were produced by placing MOF-303 from NovoMOF into a GE polymer-binder system comprised of a mixture of poly(vinyl alcohol) and poly(acrylic acid) (OBrien et al., 2022) and flowing the polymer MOF solution over the interior tube surface and subsequently curing the solution. The tubes used for these experiments were 3D-printed from Inconel. The binder did not impact the crystallinity or porosity of the MOF-303 (as shown via powder X-ray diffraction analysis and adsorption isotherms shown in the SI) and only reduced the water loading by the equivalent mass of binder added to the MOF.

3. Results and discussion

3.1. Adsorption rates collected with CSFR

During a diffusion experiment, the MOF sample was first equilibrated with a known amount of water, after which the concentration was oscillated sinusoidally, and the effluent was monitored to observe the corresponding oscillations in effluent amplitude. The effluent amplitude is diminished relative to the inlet amplitude due to adsorption occurring. The ratio of the inlet and effluent amplitudes can be calculated and a single data point can be placed on a plot of amplitude versus frequency. The process is repeated for numerous frequencies and several data points are produced. The shape of the data points as plots of amplitude versus frequency are sensitive to the mechanism of the adsorption that is occurring and with accurate models for these mechanisms, the diffusion rates can be determined.

Shown in Fig. 1 are the ratios of the effluent to feed amplitude for several MOF samples and several different humidities, all at room temperature. The diffusion rate data for MOF-303 and MOF-333 are shown in Fig. 1a and 1b, respectively, where these materials differ only in their linker composition with MOF-303 comprised of a pyrazole (1H-pyrazole-3,5-dicarboxylate) and MOF-333 comprised of a furan (furan-2,4-dicarboxylate). Shown in Fig. 1c is the diffusion data for a multivariate (MTV) MOF where the linkers are in a 50/50 ratio, which is designated 4/4-MTV-MOF, as reported previously.

Along with these data points are lines fit to the data corresponding to the micropore diffusion model, Eq. (5), and the linear driving force model, Eq. (6). Each model fit at every humidity produces an adsorption kinetic rate parameter, and thus the extracted parameters are based on several oscillating adsorption experiments repeated at several different frequencies.

As shown in Fig. 1, there are some differences between the quality of the micropore and LDF model fits. For example, for MOF-333 shown in Fig. 1b, the LDF fits the data reasonably well until the humidity approaches 20 %, at which point deviations between the LDF model and the data are observed at high frequencies. To examine this in more detail, Fig. 2a shows the high-frequency region of Fig. 1b, and it can be seen that the 20 and 22 % data sets illustrate significant differences between the LDF and micropore models with the LDF model showing a distinctly different shape compared to the data. When the LDF model is not required to fit data at higher frequencies this shape becomes more pronounced as shown by the 60 and 80 % RH data in Fig. 1b. The deviations between the LDF and the micropore models are also found near 15 % RH for 4/4-MTV-MOF and 12 % for MOF-303 coinciding with the steep portion of the isotherms of these materials. In general, the data show that the LDF model can approximate the micropore model and that

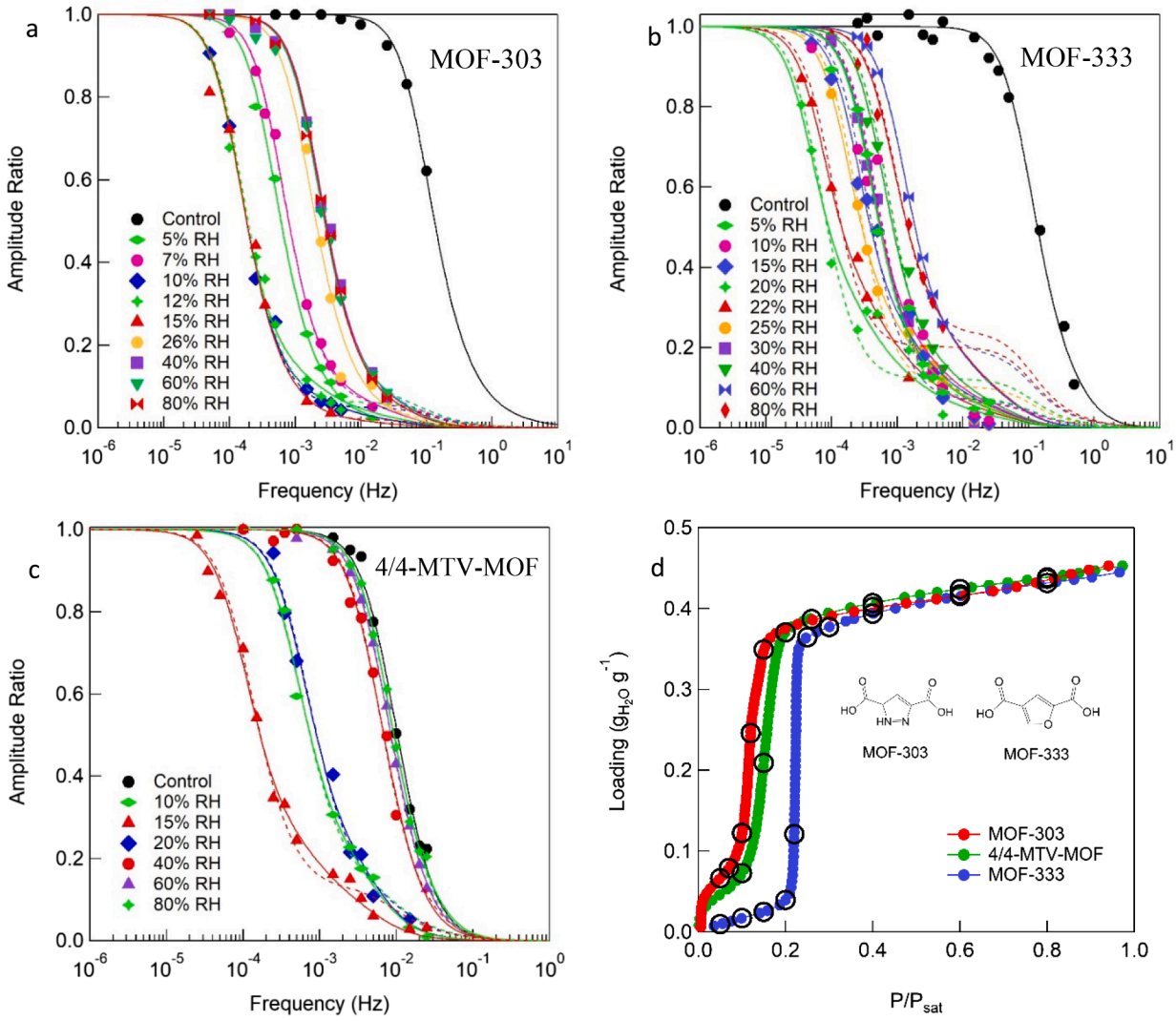

Fig. 1. Frequency response curves for (a) MOF-303 (b) MOF-333, (c) 4/4-MTV-MOF. The dashed lines are the LDF model and solid lines are the micropore diffusion model (d) Isotherms from Hanikel *et al.* where circles indicate where diffusion measurements were completed (Hanikel et al., 2019; Hanikel et al., 2021).

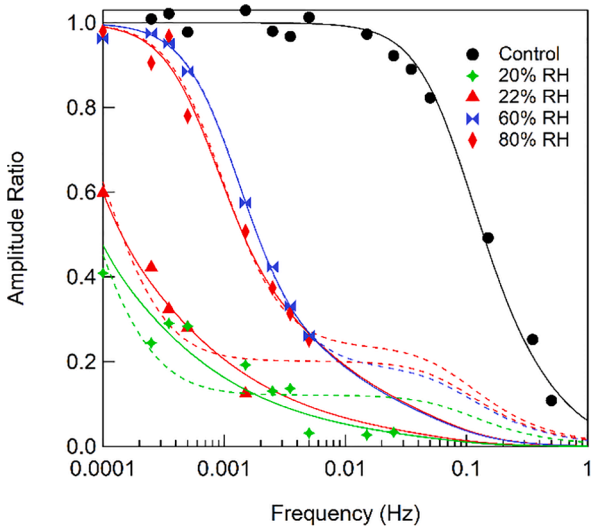

Fig. 2. Data from Fig. 1b for MOF-333 showing the deviation in the LDF and micropore models for a selection of frequencies. To ensure clarity, not all data in Fig. 1b is shown.

the error associated with the LDF assumption is most prevalent where the isotherm is the steepest.

When measuring adsorption kinetics, it can be challenging to isolate the impacts of thermal effects and these effects must be considered carefully for both flow-through and batch adsorption kinetic experiments. The milligram sample size and flow-through design of CSFR minimize these impacts and the assumption of isothermal conditions can, in many cases, be made. (Hossain and Glover, 2019; Yasuda, 1976; Wang et al., 2003; Wang and LeVan, 2008; Brandani et al., 1998; Ruthven et al., 1980; Ruthven and Lee, 1981; Giesy et al., 2012) To confirm this assumption, a comparison was made between the micropore diffusion model, and the non-isothermal micropore diffusion model as shown in Fig. 3. Both the non-isothermal and isothermal models fit the data equally well and result in nearly identical mass transfer rates. The isothermal assumption is likely valid because the adsorbed component is present only in trace amounts and therefore the rate of heat generation is dwarfed by the convection of heat away from the sorbent.

The extracted diffusion rates for each MOF as a function of relative humidity are plotted in Fig. 4. The results in Fig. 4 are significant because they show that reticular chemistry can tailor the diffusion rate of a material allowing for engineering optimization between uptake and rate that has not been readily possible with other materials. In this case, the substitution of a pyrazole for a furan in the linker is a change of only

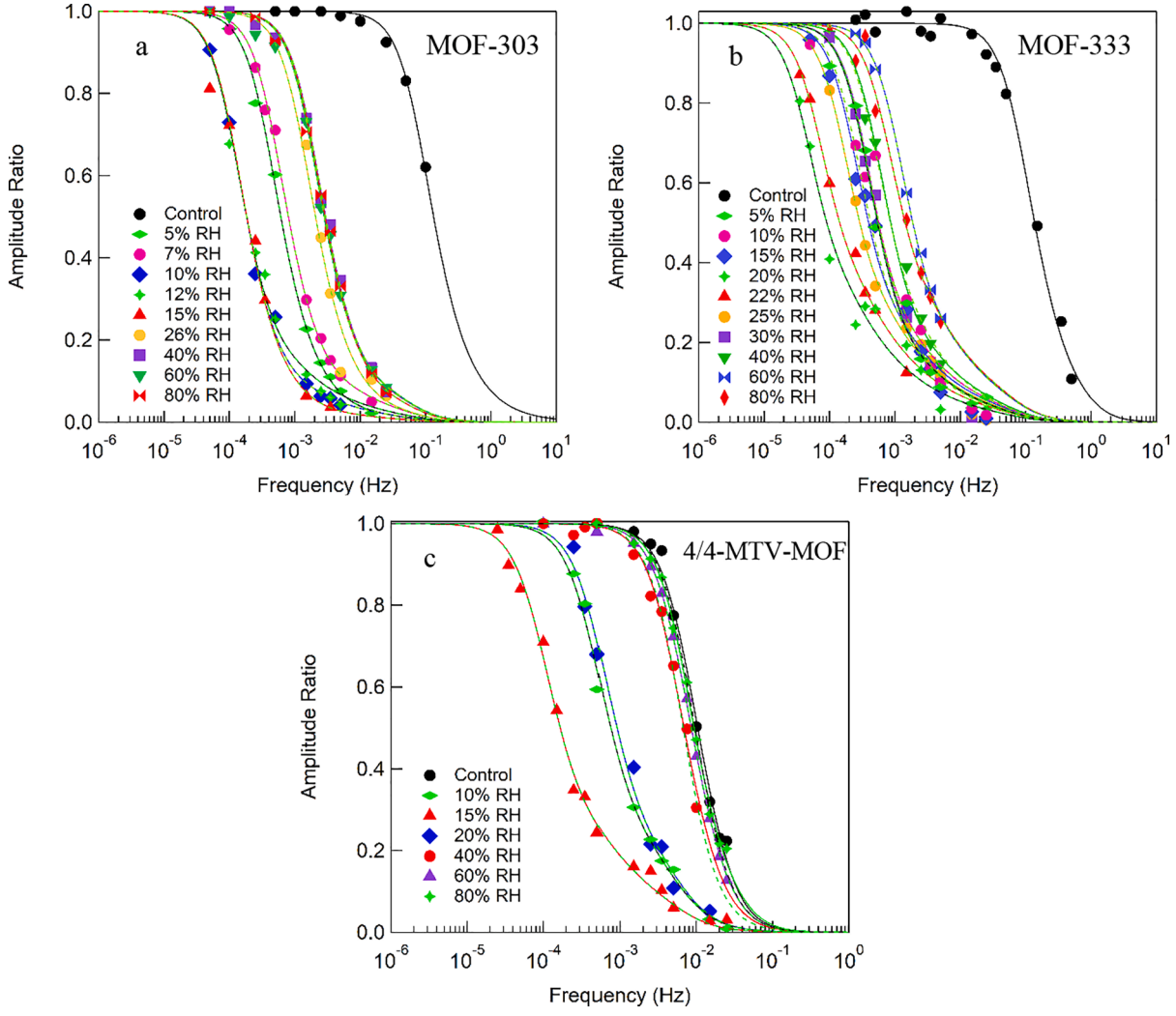

Fig. 3. A comparison of the non-isothermal diffusion model (dashed) to the isothermal diffusion model (solid) for (a) MOF-303, (b) MOF-333, and (c) 4/4-MTV-MOF. The data shows that the isothermal model fits equally well as the non-isothermal model.

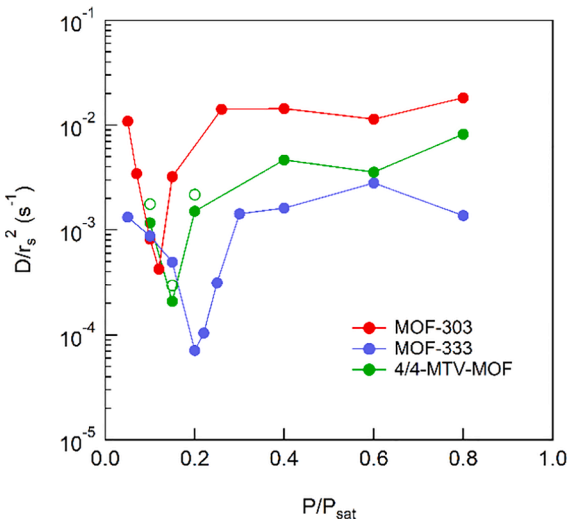

Fig. 4. Diffusion time constant as a function of concentration. The minimum in the diffusion rate is seen to correlate with the steep uptake step in the isotherm. Lines are guides for the eye. For the MTV material, a replicate data set was collected as shown with open green circles where the same sample was characterized a second time to illustrate the reproducibility of the CSFR data. (For interpretation of the references to colour in this figure legend, the reader is referred to the web version of this article.)

a few atoms that provides macroscopic changes on the adsorption kinetics of water in the MOF. While previous adsorbents, such as zeolites and carbon molecular sieves, have been designed to sieve out particular molecules for a separation, these results show that MOFs provide a means of not simply excluding molecules but rather tailoring the speed of their travel through a porous solid. For example, the minimum water diffusion rate in MOF-333 is approximately a decade slower than MOF-303.

Fig. 4 also shows that a minimum in the diffusion rates occurs that corresponds to the steepest portions of each MOF isotherm with MOF-303 having significant uptake near 10 % RH, MOF-333 having a step uptake closer to 20 % RH, and the 4/4-MTV-MOF with its uptake between these two materials. Although the change in the MOF linker is small, it has a large impact on the isotherm, and appropriately, a large impact on the diffusion rate. Likewise, the impact of the isotherm slope on the observed diffusion rate needs to be considered when explaining the observed minimum in the diffusion and is captured by calculating the corrected diffusivity in Eq. (2).

This equation shows that the observed transport diffusivity is a function of molecular mobility, termed the corrected diffusivity, and the slope of the adsorption isotherm. To examine this in more detail, the slope of the isotherm at each loading where the diffusion data was collected was calculated by linear interpolation of the isotherm data and used to determine the corrected diffusivity. Fig. 5 compares the transport and the corrected diffusivities as well as the adsorption isotherm and shows that the transport diffusivity minimum shown in Fig. 4 corresponds to the steep portion of the adsorption isotherm. However, the

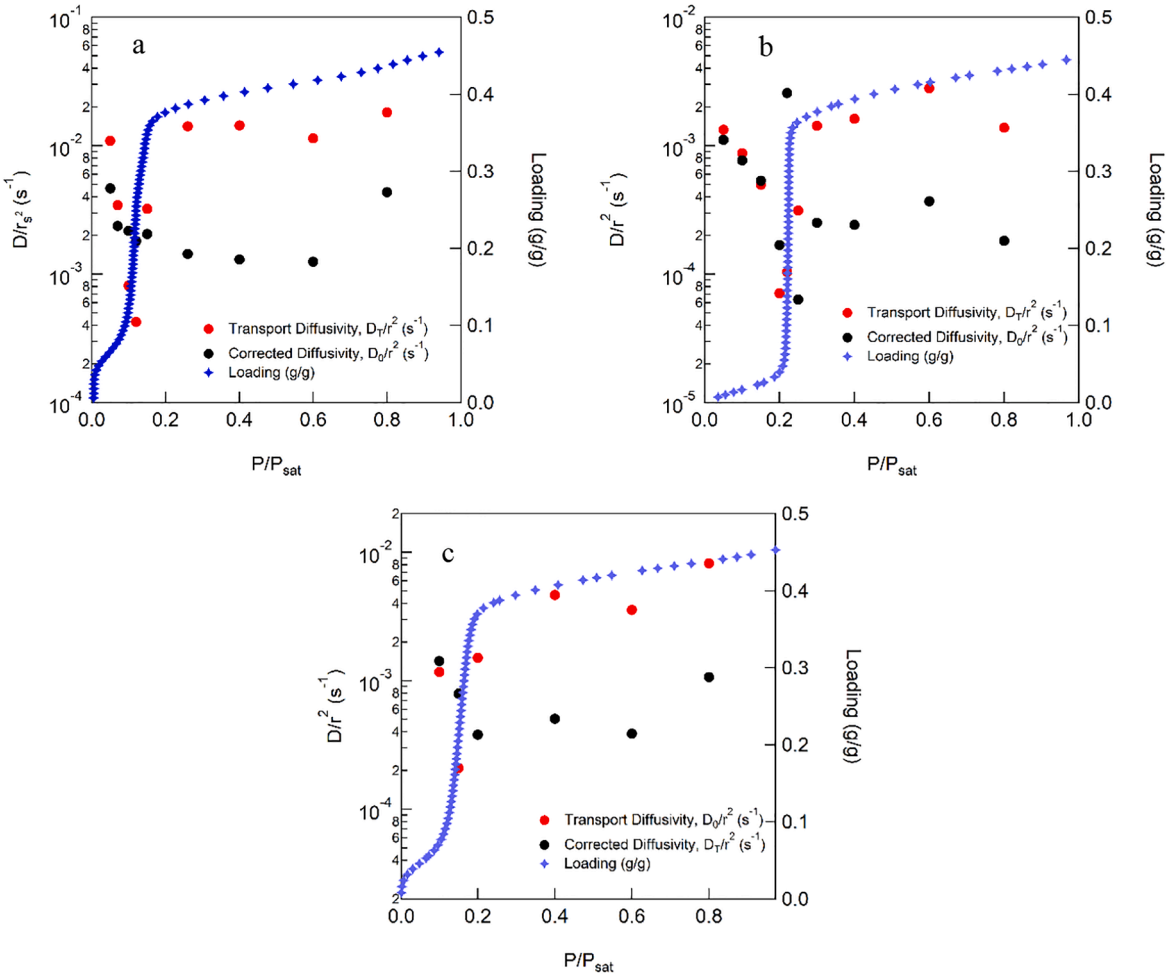

Fig. 5. Corrected and transport diffusivities for water in (a) MOF-303, (b) MOF-333, and (c) 4/4-MTV-MOF, overlayed with adsorption isotherms to illustrate the impact of equilibrium effects on transport diffusion measurements. Isotherms as from Figure 1 (Hanikel et al., 2019; Hanikel et al., 2021).

corrected diffusivity shows significantly less variability as a function of humidity compared to the transport diffusivity.

The corrected diffusivity for MOF-303 and 4/4-MTV-MOF are fairly constant, with only slight decreases in molecular mobility at very low loadings. The data for MOF-333 are slightly more scattered with the largest variation occurring at the steepest point in the adsorption isotherm. This result is consistent with the very steep slope in this region impacting the corrected diffusivity calculations.

A key portion of this comparison shows that the observed minimum in transport mobility is occurring not because of a large change in molecular mobility, but rather because of a significant change in the adsorption isotherm loading that is occurring at the given RH. This distinction is important because it helps ensure that when discussing the performance of these MOFs that the observed rate behavior is attributed to both thermodynamics and kinetics. Additionally, while this distinction is helpful to understanding the materials, the transport diffusivity that reflects the combined thermodynamic and mobility effects remains the rate that will govern diffusion processes in these materials.

This observation, that nonlinearity in the adsorption isotherm strongly influences trends in the diffusion coefficient, is consistent with observations in the literature, particularly in the adsorption of condensable vapors. (Brandani et al., 1995; Jobic et al., 2004; Kärger, 2015) For example, minimums in diffusivity in both activated carbon and UiO-66 MOF have been reported. (Hossain and Glover, 2019; Glover et al., 2008) For UiO-66, it has been shown that a constant corrected diffusivity can be assumed and the isotherm slope can be used to predict the concentration dependence of the diffusion data with reasonable accuracy. (Hossain and Glover, 2019) The results in Fig. 5 are consistent with the results shown for UiO-66 as the data in Fig. 5 shows a nearly constant corrected diffusivity and the isotherm slope driving the observed minimum in the diffusion data.

Regarding the diffusive length scale, the rates measured by CSFR are captured as $\frac{D_s}{r^2}$ and information about r^2 is not provided in these experiments. It is possible that the diffusional path length is the entire MOF crystal or a small collection of MOF crystals, but in this case, MOFs provide a unique opportunity to examine the impact of adsorbate size on diffusion because crystals of the same chemical composition and crystalline phase can be produced in various sizes.

Therefore, to better understand the controlling diffusion length scale and the trends between materials, MOF-303, MOF-333, and 4/4-MTV-MOF were synthesized again but with larger crystal sizes as shown in Fig. 6. For comparison, the MOF-303 material examined initially is shown in Fig. 6a and shows agglomerations of smaller MOF crystals into larger clusters as compared to Fig. 6d that shows MOF crystals that are closer to 20 μm individually. The raw frequency response data is shown in Fig. 7a and the diffusion rates extracted from each of these experiments are shown in Fig. 7b, where the data from the original samples from Fig. 4 are replotted for comparison. The diffusion data on the larger crystals are effectively the same as the original materials. Given that the MOFs have the same composition and crystalline structure, it can be assumed that the diffusion rate, D_s, was the same in these materials, and with $\frac{D_s}{r^2}$ appearing to have nearly identical values, that the diffusive length r^2 was similar for both sets of materials. It is possible that the smaller crystals are forming aggregates with similar diffusive lengths as either the larger crystals, or both samples produced aggregates of similar sizes regardless of crystal size.

Beyond noticing that for the crystal sizes studied the diffusion rates are effectively the same, broader conclusions are somewhat difficult because there are only 6 samples compared and only 3 similar data points. It is interesting to note, however, that the crystal sizes in the SEM

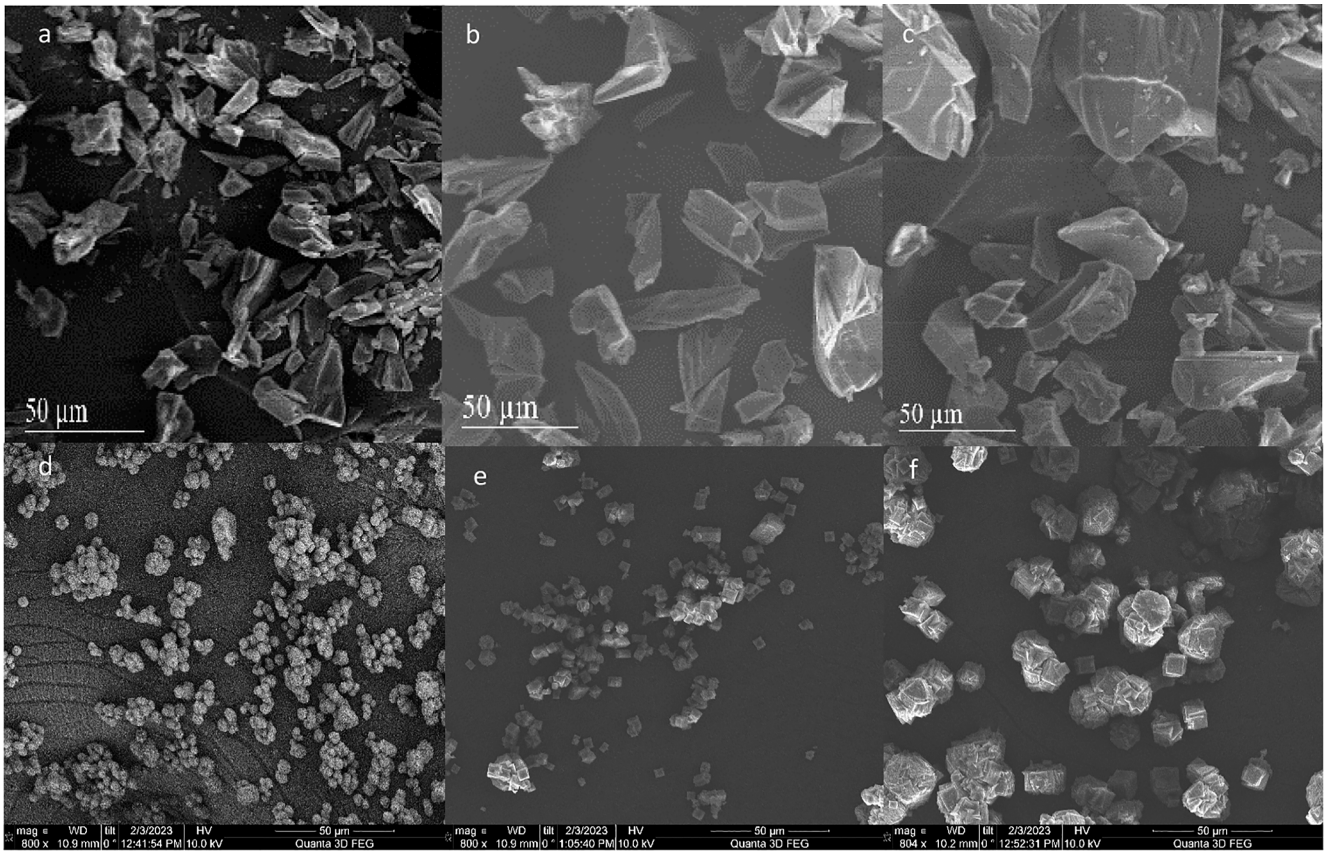

Fig. 6. SEM images of large crystals of (a) MOF-303, (b) 4/4-MTV-MOF, (c) MOF-333, and powders of (d) MOF-303, (e) 4/4-MTV-MOF, and (f) MOF-333. The crystal size follows the trend of MOF-333 > 4/4-MTV-MOF > MOF-303 and the crystals in the powders appear to form aggregates of similar size to the individual crystals in (a-c).

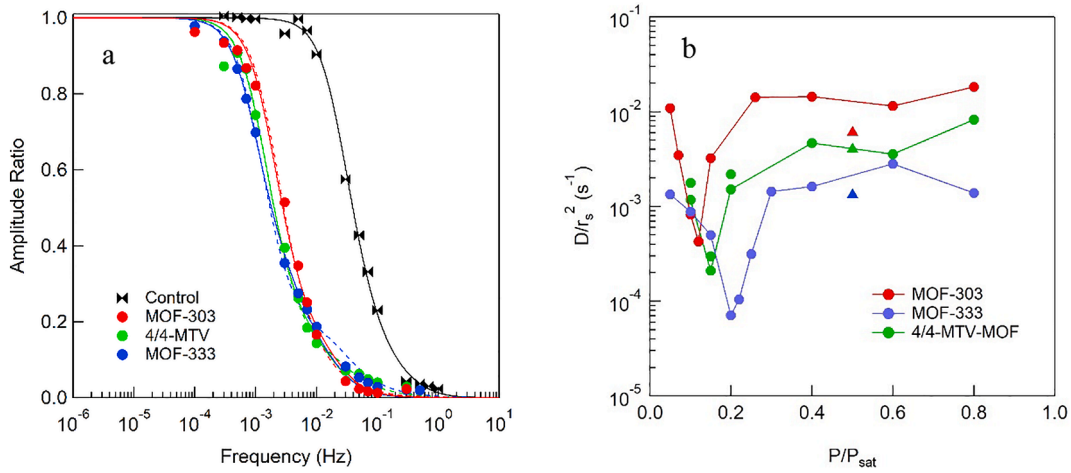

Fig. 7. (a) CSFR data and (b) diffusion rates in larger crystal MOF samples (triangles), compared with powders (circles).

follow the general trend of MOF-333 > 4/4-MTV-MOF > MOF-303, which is consistent with the observed transport diffusion rates with MOF-303 having the fastest rates and MOF-333 the slowest. However, these results only highlight that more work is required to fully understand the impact of MOF crystal size on gas diffusion rates.

In addition to measuring diffusion data at ambient temperature, we also measured the diffusion rates of water at 40 °C on MOF-303 as shown in Fig. 8. As expected, the minimum in the diffusion data shifts slightly to a higher RH, consistent with the water isotherm at 40 °C, shown in the SI. The rate of diffusion at 40 °C are faster than those of 25 °C, as expected, and provides insight into the change of adsorption rates that will take place during heated desorption steps in water-harvesting systems. Tabulated mass transfer data for each MOF is reported in the SI.

To provide perspective on the diffusion rates of water into these materials, they were compared to the water diffusion rates for activated carbon, which we have also measured using CSFR. (Glover et al., 2008) The results are shown in Fig. 9a and show that even though a minimum in the diffusion occurs, the adsorption rate of water in MOF-303 is fast throughout the adsorption process compared to activated carbon. The diffusion data have also been plotted versus loading as shown in Fig. 9b, which shows that the minimum diffusion rate extends over a wide range of loadings illustrating that in many cases the water transport diffusion rate is nearly constant.

3.2. Application of adsorption rate data

During the evaluation of new materials, it is common to complete breakthrough measurements to determine adsorbate loading and separation performance. (Glover and Mu, 2018; Britt et al., 2009; Grant Glover et al., 2011) Concentration-dependent mass transfer data and equilibrium isotherms form the foundation for understanding and modeling this type of behavior. As a broadly applicable example of evaluating a MOF for water harvesting, MOF-303 was pressed into pellets, without a binder, and ambient air was pulled through the MOF-303 adsorption bed. The inlet and effluents of the breakthrough system were monitored to produce the breakthrough curve shown in Fig. 10. This breakthrough test was conducted on 3.11 g of MOF-303 in a tube that was 1.5 in. in diameter with additional details in the SI.

It is important to note that the unique shape of the breakthrough curve shown in Fig. 10 occurs not because of mass transfer effects, but rather because of the shape of the adsorption isotherm. It has been shown by others that this type of behavior is consistent for adsorbents with Type IV and V isotherms and occurs because of inflection points in those isotherms. Specifically, isotherms of this type have transitions from favorable to unfavorable adsorption that results in changes in the breakthrough curve from a more shock-like curve to a more dispersed curve. (LeVan and Carta, 2008) Others have also documented this behavior on water adsorption on aluminum fumarate breakthrough curves. (Bozbiyik et al., 2017) Therefore, because the unique shape is a result of the isotherm, and the isotherm shape can be controlled by

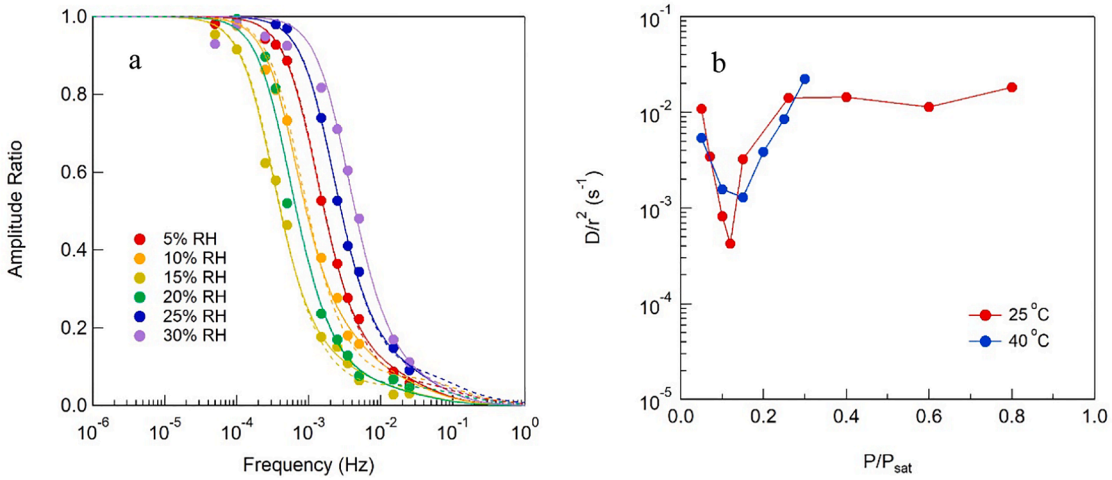

Fig. 8. Water diffusion rate vs RH for MOF-303 at 40 °C (a) CSFR data and (b) diffusion rates for MOF-303.

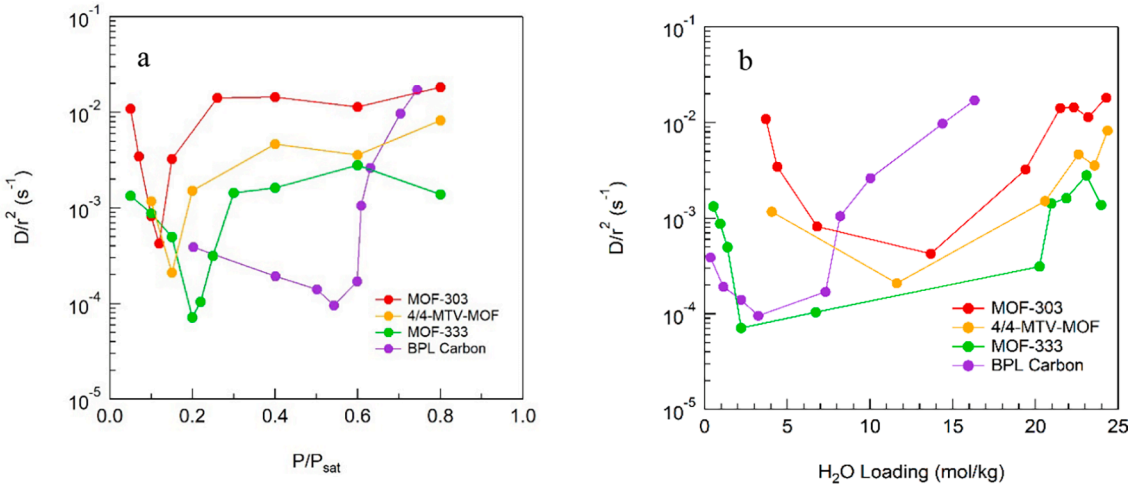

Fig. 9. A comparison of the diffusion rates of water in MOF-303, MOF-333, 4/4-MTV-MOF, and BPL Carbon as a function of (a) RH and (b) loading. Lines are guides for the eye.

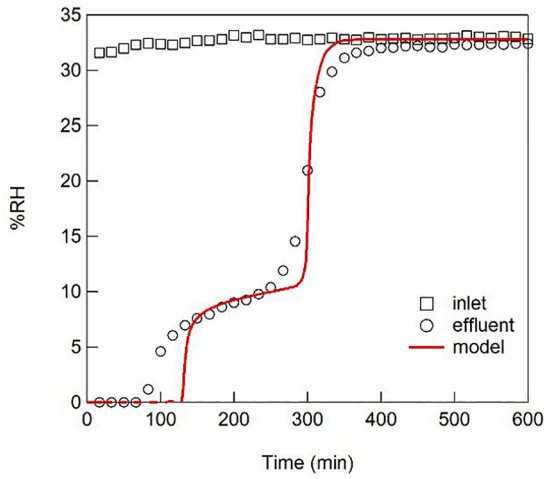

Fig. 10. Experimental Breakthrough Curve (points) and COMSOL model (line).

atomic-scale changes to the MOF link, reticular chemistry provides a way to tune this behavior that has traditionally not been possible.

A COMSOL Multiphysics model of the breakthrough curve in Fig. 10 was developed using a 2D axisymmetric porous domain to represent the packed bed (details provided in the SI). As shown in Fig. 10, the model captures the breakthrough behavior and includes the atypical breakthrough behavior resulting from the isotherm.

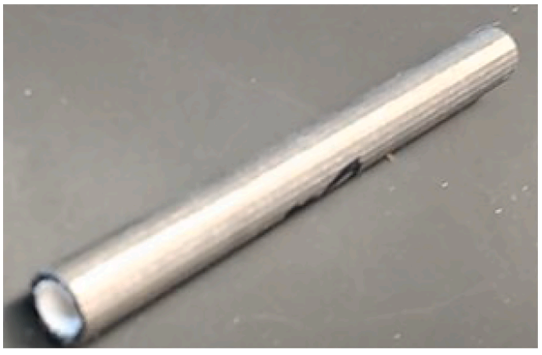

Fig. 11. The 3D printed Inconel ¼" tube, 6.395 cm long, was made and coated with a 0.21 mm thick MOF coating for breakthrough testing and modeling.

Beyond a packed-bed design, it is also possible to envision water-harvesting devices that utilize coatings of MOFs on surfaces. Therefore, to gain a better understanding of the role of diffusion resistance and water capture in these systems, MOF-303 was contained in a polymer and coated on a tube wall (Fig. 11).

3.3. Macropore diffusion rates collected with CSFR

Because the MOF in Fig. 11 is deployed in a polymer matrix, it was uncertain if micropore diffusion or macropore diffusion would be the controlling mass transfer mechanism. Therefore, CSFR was used to quantify a piece of the MOF-303 polymer coating. As discussed above, the micropore and macropore diffusive models have the same mathematical form, therefore, measurements were performed on three separate pieces of the composite of varying diameters. As seen in Fig. 12, the response curves show a dependency on particle size, which confirms a macropore limitation (Giesy and LeVan, 2013; Hossain et al., 2019; Tovar, 2016).

Measurements of the macropore diffusion rate were completed at 10, 40, and 60 % RH on the largest piece of composite and the results are shown in Fig. 13. The data show that the response curves depend on RH, but the macropore diffusivity of the polymer composite is less dependent on gas concentration than the micropore diffusion rates for MOF-303,

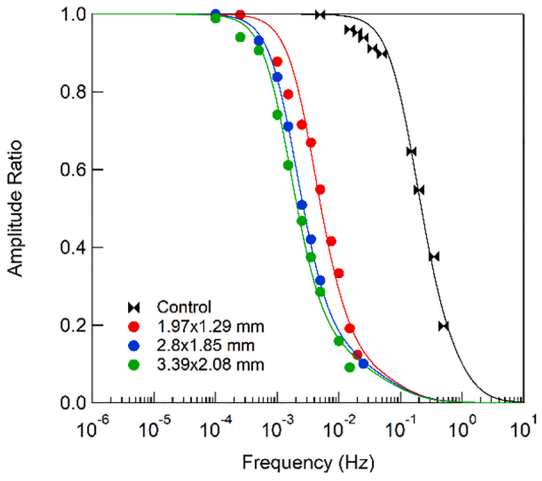

Fig. 12. CSFR response curves for 3 pieces of the MOF-303/polymer composite at 40 % RH and 25 °C.

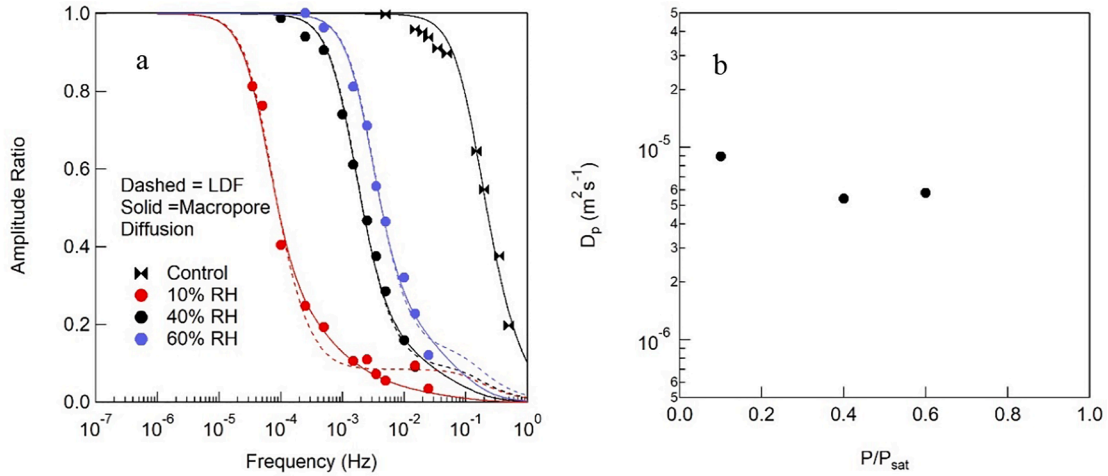

Fig. 13. (a) CSFR response curves and (b) extracted macropore diffusivities as a function of RH for a 3.39x2.09 mm piece of MOF-303/polymer composite at 25 °C.

MOF-333, or 4/4-MTV-MOF. This is because the response reflects the effective diffusivity, which for systems with nonlinear isotherms is generally a function of concentration. In particular, the effective diffusivity is defined as (Ruthven, 1984)

$$D_e = \frac{D_p}{\left(\frac{\rho_p K}{\varepsilon_p} + 1\right)} \tag{19}$$

and it can be seen that if the macropore diffusivity is constant, the effective diffusivity depends on concentration because the isotherm slope is a function of concentration. When this is accounted for, a value for the macropore diffusivity that is independent of concentration is obtained and is only a function of the macropore structure of the material in which diffusion is occurring. Because this value of D_p is intrinsic to the material and geometry independent, it was calculated using the density (183.2 kg/m^3) and porosity (0.584) of the piece of composite. The porosity was determined using

$$\varepsilon_p = 1 - \frac{\rho_p}{\rho_s} \tag{20}$$

where ρ_s is the skeletal density, 440 kg/m^3. The isotherm slope in the calculation of D_p was obtained from the CSFR fitting process.

With the diffusion quantified, a breakthrough test was completed using the coated tube, and the results were modeled using COMSOL, which are shown in Fig. 14. In the tube case, an additional diffusional resistance from the surface of the coating to the tube wall was included in addition to a micropore diffusion parameter. In this way, the tube model accounts for the mass transfer of water through the tube (convective flow), from the coating surface to the micropores (macropore diffusion), and from the micropores to the adsorption site (micropore diffusion). For computational simplicity, the micropore diffusion was described using the MOF-303 LDF coefficients from CSFR measurements completed on the pure powder of smaller crystals.

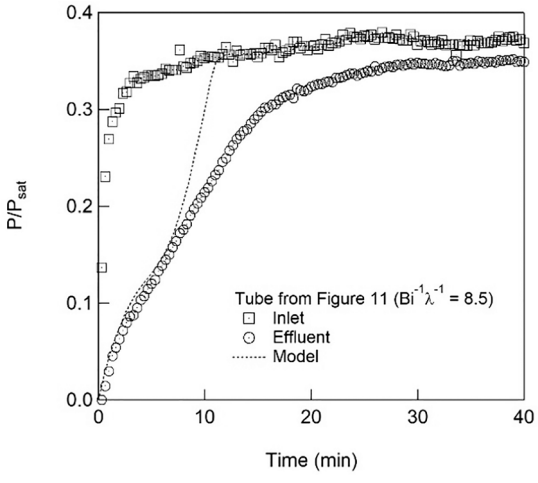

Fig. 14. MOF-303 coated-tube, water adsorption, breakthrough experimental data (points) and model (lines).

The modeling results accurately predict the breakthrough behavior and show that CSFR can provide values suitable for modeling not only packed-bed behaviors, but also coated tubes and other film-based contactors.

Isotherms were collected for both the pure powder MOF-303, the polymer film made using MOF-303, and pieces of MOF-303 contained in a binder but not in a film, and these isotherms are reported in the SI. The average of the experimental isotherms for the film and pieces were used to model the capacity of the coating in the tube. The model is in good agreement with the breakthrough data. Breakthrough data and model predictions for 3 additional tubes are reported in Figure S12 and all show good agreement between the models and the experiments.

3.4. Diffusion versus convection numerical modeling

To understand the different adsorption regimes of the simple tube-based water harvester, the COMSOL model was used to explore the impact of coating thickness on the water capture rate, and two limiting regimes were identified as shown in Fig. 15. While this problem has been examined in previous work, (Sartory, 1978; Tereck et al., 1987) this work extends the treatment to finite mass transfer rates in sorbent layers where thickness cannot be neglected. In Fig. 15, red is used to represent high water content close to the feed concentration, and blue is used to represent dry conditions. In the first case, the coating thickness was 0.5 mm and the flow rate was 0.177 m/s whereas in the second case, the coating thickness was increased to 1 mm with a flow rate of 5 m/s. As shown in Fig. 15a, the flow rate of water vapor through the tube in this configuration is slow enough such that all the water that enters the tube is adsorbed and no water exits the effluent of the tube. In this case, the tube is behaving similarly to the packed bed breakthrough experiment shown previously. However, in this case, a large fraction of the MOF coating is not being utilized and is simply waiting for water vapor to move through the tube. This type of operational regime is important when the breakthrough of the adsorbate cannot be allowed, such as toxic gas filtration, flue gas filtration, or chemical separations, and depending on the type of water-harvesting system design, could be important for some water-harvesting systems.

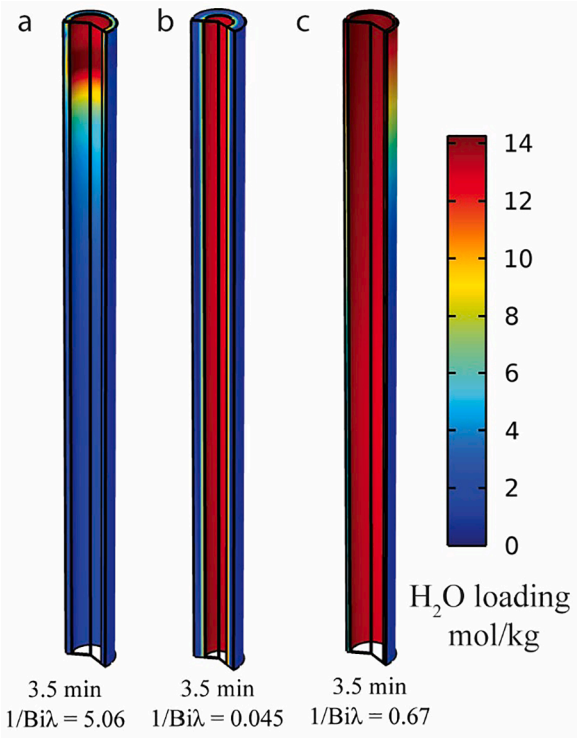

Fig. 15. Long-time concentration profiles for adsorption in the coated tube under (a) convection limited, (b) diffusion limited, and (c) intermediate rate limiting regimes.

In the second case, shown in Fig. 15b, water vapor is present in a concentration equal to the feed concentration throughout the tube, and in this configuration, the feed water concentration is always equal to the effluent water concentration. The figures show that with the water vapor always constant, the mass transfer is now limited to the diffusion rate of water into the film layer. In this case, all the MOF is being used, but the rate of the adsorption process is now limited by the mass transfer rate into the adsorptive layer, and depending on the system design, this could be the macropore diffusion rate, such as in this example system, or the micropore diffusive limit if the polymer offered no resistance to mass transfer relative to the micropore rate. In Fig. 15c, there is an intermediate case illustrated where water flows out of the tube, but a slower wave of water adsorption progresses axially through the MOF layer.

3.5. Diffusion and convection time scale and limiting cases

With these results in mind, it would be helpful to examine the process more generically and determine when convection or macropore diffusion is governing the adsorption of water in the system by examining the relative timescales of each process. For this analysis, the flow through a tube whose inner walls are coated with a layer of sorbent is considered. To formulate a model, the convective flux down the channel, the diffusive flux into (or out of) the adsorbent, need to be described, as well as the time-dependent concentration profile down the flow channel.

First, a mass balance (additional details in the SI) was written on the air channel as

$$\frac{\partial\theta}{\partial\tau}=\frac{1}{Pe}\frac{\partial^2\theta}{\partial\xi^2}+\frac{1}{Pe\gamma}\frac{1}{\psi}\frac{\partial}{\partial\psi}\left(\psi\frac{\partial\theta}{\partial\psi}\right)-\frac{\partial\theta}{\partial\xi} \tag{21}$$

where $\theta=\frac{C}{C_0}$ is the dimensionless gas phase concentration of water, related to the inlet concentration C_0, $\tau=\frac{tv}{L}$ is the dimensionless time where t is time, v is velocity, and L is the length of the tube, $\psi=\frac{r}{R}$ is the dimensionless radial coordinate where R is the hydraulic radius of the tube, $\gamma=\frac{R}{L}$ is the aspect ratio of the air channel, $\xi=\frac{z}{L}$ is the dimensionless axial coordinate, and $Pe=\frac{vL}{D_{H_2O,air}}$ is the Peclet number. Likewise, for the MOF domain

$$\frac{\partial\theta}{\partial\tau}=\frac{1}{\eta}\frac{\partial}{\partial\eta}\left(\eta\frac{\partial\theta}{\partial\eta}\right)+\lambda^2\frac{\partial^2\theta}{\partial\xi^2}-D\ddot{a}\Lambda(1-\phi) \tag{22}$$

where $\theta=\frac{C}{C_0}$ is the dimensionless gas phase concentration of water, related to the inlet concentration C_0, $\tau=\frac{tD_m}{\delta^2}$ is the dimensionless time where t is time, δ is the sorbent layer thickness, and D_m is the macropore diffusivity of water in the sorbent layer, $\eta=\frac{r}{\delta}$ is the dimensionless radial coordinate, $\xi=\frac{z}{L}$ is the dimensionless axial coordinate, $\lambda=\frac{\delta}{L}$ is the aspect ratio of the coating, $D\ddot{a}=\frac{k\delta^2}{\varepsilon_m D_m}$ is the ratio of micropore diffusion rate, given by the LDF coefficient k, to macropore diffusion rate, $\Lambda=\rho\frac{n^*}{C_0}$ is the partition ratio that often appears in packed bed analysis, (LeVan and Carta, 2008) where r is sorbent density, n* is the equilibrium loading at C_0, the inlet concentration, and $\phi=\frac{n}{n^*}$ represents fractional loading.

Following this analysis, a balance at the interface between the air and the MOF gives

$$\left.\frac{dC}{dt}\right|_{airside}=\varepsilon_m\left.\frac{dC}{dt}\right|_{MOFside} \tag{23}$$

Using the above equations and defining the following dimensionless parameter gives

$$Bi=\frac{v\delta}{\varepsilon_m D_m} \tag{24}$$

$$\frac{1}{Pe}\frac{\partial^2\theta}{\partial\xi^2}+\frac{1}{Pe\gamma}\frac{1}{\psi}\frac{\partial}{\partial\psi}\left(\psi\frac{\partial\theta}{\partial\psi}\right)-\frac{\partial\theta}{\partial\xi}=\frac{1}{Bi\lambda}\frac{1}{\eta}\frac{\partial}{\partial\eta}\left(\eta\frac{\partial\theta}{\partial\eta}\right)+\frac{\lambda}{Bi}\frac{\partial^2\theta}{\partial\xi^2}-\frac{D\ddot{a}\Lambda}{Bi\lambda}(1-\phi) \tag{25}$$

which, upon rescaling the ψ derivatives to η ones by multiplying the ψ containing term by $\frac{R}{\delta}$, collecting like terms, and simplifying, gives

$$0=\left(\frac{1}{Bi\lambda}-\frac{1}{Pe\lambda}\right)\frac{1}{\eta}\frac{\partial}{\partial\eta}\left(\eta\frac{\partial\theta}{\partial\eta}\right)+\left(\frac{\lambda}{Bi}-\frac{1}{Pe}\right)\frac{\partial^2\theta}{\partial\xi^2}-\frac{D\ddot{a}\Lambda}{Bi\lambda}(1-\phi)+\frac{\partial\theta}{\partial\xi} \tag{26}$$

Eq. (26) that can be used to understand when diffusion or convection is dominating adsorption. In the following, the contributions of axial and radial dispersion are neglected since the term $\frac{1}{Pe}$ can be assumed to be very small. Thus, Eq. (26) can be simplified as

$$0=\frac{1}{Bi\lambda}\frac{1}{\eta}\frac{\partial}{\partial\eta}\left(\eta\frac{\partial\theta}{\partial\eta}\right)+\frac{\lambda}{Bi}\frac{\partial^2\theta}{\partial\xi^2}-\frac{D\ddot{a}\Lambda}{Bi\lambda}(1-\phi)+\frac{\partial\theta}{\partial\xi} \tag{27}$$

for the purposes of the following treatment. Indeed, it is also possible to neglect the term $\frac{\lambda}{Bi}\frac{\partial^2\theta}{\partial\xi^2}$ entirely, and the governing terms in the above are the groups $\frac{1}{Bi\lambda}$ and $\frac{D\ddot{a}\Lambda}{Bi\lambda}$, as will be made apparent in the following.

3.6. Limiting behaviors

There are 3 limiting cases in this analysis. The process can be limited by the rate of convection down the tube, the rate of diffusion into the layer, or the rate of adsorption (which is typically a micropore diffusion limit).

The term $\frac{1}{Bi\lambda}$ expands to $\frac{L\varepsilon_m D_m}{v\delta^2}$ and can be seen to be the ratio of the macropore diffusion rate into the layer, $\frac{\varepsilon_m D_m}{\delta^2}$, vs the convection rate down the tube axially, $\frac{v}{L}$. Thus, a large value implies that diffusion into the layer is faster than convection and the limiting factor is the convection time down the tube. In this case, the bed is starved of feed and the uptake is limited by how quickly moisture is fed into the tube via convection. In contrast, small values imply that convection overwhelms diffusion, the bed is flooded with feed, moist air is blown out of the

effluent of the tube, and the uptake rate is limited by how quickly moisture can diffuse into the layer.

Using these groups to characterize Fig. 15 shows 15a has a $\frac{1}{Bi\lambda}$ of 5.06, indicating a convective limit when compared to Fig. 15b, which has a $\frac{1}{Bi\lambda}$ of 0.045, showing the diffusion limit. In Fig. 15c, the value of $\frac{1}{Bi\lambda}$ is 0.67, showing an intermediate case. Interestingly, in Fig. 15c it appears as if water vapor is being lost out of the effluent, but simultaneously the concentration front proceeds axially as a shock front through the coating layer and not radially outward as in Fig. 15b. Understanding how to balance these rates is important as it optimizes the time waiting on radial diffusion into the coating and energy spent overfeeding the adsorbent.

The term $\frac{D\ddot{a}\Lambda}{Bi\lambda}$ expands to $\frac{k\rho n^* L}{vC_0}$ and can be seen to be the ratio of adsorption rate, $\frac{k\rho n^*}{C_0}$, to convection rate, $\frac{v}{L}$. This value is always very large for the cases examined.

A third dimensionless ratio can be obtained by taking the ratio of these two, namely the ratio of adsorption rate, $\frac{k\rho n^*}{C_0}$, to macropore diffusion rate, $\frac{\varepsilon_m D_m}{\delta^2}$. This term appears in the balance on only the MOF layer and is given by $D\ddot{a}\Lambda = \frac{k\rho n^* \delta^2}{C_0 \varepsilon_m D_m}$, and in most cases this number is also very large. Thus, in practice, there are two main limiting cases as outlined above, where either diffusion into the layer is limiting, or convection down the tube is limiting. This is consistent with the local equilibrium assumption often made when considering packed beds. (LeVan and Carta, 2008).

4. Conclusion

The impact of atom-scale changes on the adsorption kinetics was examined by comparing two isostructural MOFs, MOF-303 and MOF-333, and a multivariate MOF where the linkers are present in a 50/50 ratio, 4/4-MTV-MOF. These experiments illustrate precision molecular level control over the diffusion rates in these materials, with the ability to control the location of the minimum diffusion rate using a blend of linkers in the MOF. The concentration dependence of the diffusion rate for each of these materials shows a minimum in the diffusion rate correlating to the steep uptake step in the sorption isotherm. Calculation of the corrected diffusivity shows that this minimum occurs because of the slope in the adsorption isotherm. Additionally, CSFR experiments were used to identify the impacts of containing these materials in polymer binders by identifying when micropore and macropore resistances were dominant.

The diffusion rates were applied to model the behavior of a simple single-tube water-harvesting contactor to understand the balance between convective and diffusion time scales. A mass balance analysis was completed to identify the limiting behaviors of a water-harvesting system and to show when diffusion would provide a rate-limiting system behavior.

The results show the examination of mass transfer kinetics from the water molecule to a simple representative water-harvesting system. The data highlight the importance of understanding not only the adsorption capacity in water harvesters but also diffusion rates in MOFs materials. The results apply to a variety of different water-harvesting designs as well as other adsorption devices and shed light on the connection between atom-precision synthesis, diffusion, and process design.

Declaration of Competing Interest

The authors declare the following competing financial interest(s): O. M.Y. is co-founder of Water Harvesting Inc. and ATOCO Inc., aiming at commercializing related technologies. T.G.G. is a co-founder of ATOCO Inc. The remaining authors declare no competing interests.

Data availability

Data will be made available on request.

Acknowledgments

This material is based on work supported by the Defense Advanced Research Projects Agency (DARPA) under contract HR001-21-C-0020. Any opinions, findings, conclusions, or recommendations expressed in this material are those of the author(s) and do not necessarily reflect the views of DARPA. J.H. acknowledges financial support from the Alabama Graduate Research Scholars Program (GRSP) funded through the Alabama Commission for Higher Education and administered by the Alabama EPSCoR. This study is also supported by a Kavli ENSI Philomathia Graduate Student Fellowship and a Blavatnik Innovation Fellowship (N. H.). Helpful comments and suggestions on this work were provided by Dr. Seth Cohen (DARPA).

Appendix A. Supplementary data

Supplementary data to this article can be found online at https://doi.org/10.1016/j.ces.2023.119430.

References

Alsaedi, M.K., 2018. Atmospheric Water Harvesting by an Anhydrate Salt and Its Release by a Photothermal Process Towards Sustainable Potable Water Production in Arid Regions. Thesis. https://doi.org/10.25781/KAUST-I3517.

Bagheri, F., 2018. Performance Investigation of Atmospheric Water Harvesting Systems. Water Resour. Ind. 20, 23–28. https://doi.org/10.1016/j.wri.2018.08.001.

Bozbiyik, B., Van Assche, T., Lannoeye, J., De Vos, D.E., Baron, G.V., Denayer, J.F.M., 2017. Stepped Water Isotherm and Breakthrough Curves on Aluminium Fumarate Metal-Organic Framework: Experimental and Modelling Study. Adsorption 23 (1), 185–192. https://doi.org/10.1007/s10450-016-9847-0.

Brandani, S., Hufton, J., Ruthven, D., 1995. Self-Diffusion of Propane and Propylene in 5A and 13X Zeolite Crystals Studied by the Tracer ZLC Method. Zeolites 15 (7), 624–631. https://doi.org/10.1016/0144-2449(95)00042-5.

Brandani, S., Xu, Z., Ruthven, D., 1996. Transport Diffusion and Self-Diffusion of Benzene in NaX and CaX Zeolite Crystals Studied by ZLC and Tracer ZLC Methods. Microporous Mater. 7 (6), 323–331. https://doi.org/10.1016/S0927-6513(96)00010-7.

Brandani, S., Cavalcante, C., Guimarães, A., Ruthven, D., 1998. Heat Effects in ZLC Experiments. Adsorption 4 (3), 275–285. https://doi.org/10.1023/A:1008837801299.

Britt, D., Furukawa, H., Wang, B., Glover, T.G., Yaghi, O.M., 2009. Highly Efficient Separation of Carbon Dioxide by a Metal-Organic Framework Replete with Open Metal Sites. Proceedings of the National Academy of Sciences 106 (49), 20637–20640. https://doi.org/10.1073/pnas.0909718106.

Burtch, N.C., Jasuja, H., Walton, K.S., 2014. Water Stability and Adsorption in Metal-Organic Frameworks. Chem. Rev. 114 (20), 10575–10612. https://doi.org/10.1021/cr5002589.

Canivet, J., Fateeva, A., Guo, Y., Coasne, B., Farrusseng, D., 2014. Water Adsorption in MOFs: Fundamentals and Applications. Chem Soc Rev 43 (16), 5594–5617. https://doi.org/10.1039/C4CS00078A.

Canivet, J., Bonnefoy, J., Daniel, C., Legrand, A., Coasne, B., Farrusseng, D., 2014. Structure-Property Relationships of Water Adsorption in Metal-Organic Frameworks. New J Chem 38 (7), 3102–3111. https://doi.org/10.1039/C4NJ00076E.

Deisler, P.F., Wilhelm, R.H., 1953. Diffusion in Beds of Porous Solids. Measurement by Frequency Response Techniques. Ind. Eng. Chem. 45 (6), 1219–1227. https://doi.org/10.1021/ie50522a026.

Do, D.D., Mayfield, P.L.J., 1987. A New Simplified Model for Adsorption in a Single Particle. AIChE J. 33 (8), 1397–1400.

Eic, M.; Ruthven, D. M. Intracrystalline Diffusion of Linear Paraffins and Benzene in Silicalite Studied by the ZLC Method. In *Studies in Surface Science and Catalysis*; Jacobs, P. A., van Santen, R. A., Eds.; Zeolites: Facts, Figures, Future Part A - Proceedings of the 8th International Zeolite Conference; Elsevier, 1989; Vol. 49, pp 897–905. https://doi.org/10.1016/S0167-2991(08)61976-X.

Fathieh, F., Kalmutzki, M.J., Kapustin, E.A., Waller, P.J., Yang, J., Yaghi, O.M., 2018. Practical Water Production from Desert Air. Sci. Adv. 4 (6), eaat3198. https://doi.org/10.1126/sciadv.aat3198.

Furukawa, H., Gándara, F., Zhang, Y.-B., Jiang, J., Queen, W.L., Hudson, M.R., Yaghi, O. M., 2014. Water Adsorption in Porous Metal-Organic Frameworks and Related Materials. J. Am. Chem. Soc. 136 (11), 4369–4381. https://doi.org/10.1021/ja500330a.

Gido, B., Friedler, E., Broday, D.M., 2016. Assessment of Atmospheric Moisture Harvesting by Direct Cooling. Atmospheric Res. 182, 156–162. https://doi.org/10.1016/j.atmosres.2016.07.029.

Giesy, T.J., LeVan, M.D., 2013. Mass Transfer Rates of Oxygen, Nitrogen, and Argon in Carbon Molecular Sieves Determined by Pressure-Swing Frequency Response. Chem. Eng. Sci. 90, 250–257. https://doi.org/10.1016/j.ces.2012.12.029.

Giesy, T.J., Wang, Y., LeVan, M.D., 2012. Measurement of Mass Transfer Rates in Adsorbents: New Combined-Technique Frequency Response Apparatus and Application to CO_2 in 13X Zeolite. Ind. Eng. Chem. Res. 51 (35), 11509–11517. https://doi.org/10.1021/ie3014204.

Gas Adsorption in Metal-Organic Frameworks: Fundamentals and Applications; Glover, T. G., Mu, B., Eds.; CRC Taylor & Francis, 2018.

Glover, T.G., Wang, Y., LeVan, M.D., 2008. Diffusion of Condensable Vapors in Single Adsorbent Particles Measured via Concentration-Swing Frequency Response. Langmuir 24 (23), 13406–13413. https://doi.org/10.1021/la802222r.

Glueckauf, E., 1955. Theory of Chromatography. Part 10.—Formulæ for Diffusion into Spheres and Their Application to Chromatography. Trans. Faraday Soc. 51, 1540–1551.

Grant Glover, T., Peterson, G.W., Schindler, B.J., Britt, D., Yaghi, O., 2011. MOF-74 Building Unit Has a Direct Impact on Toxic Gas Adsorption. Chemical Engineering Science 66 (2), 163–170. https://doi.org/10.1016/j.ces.2010.10.002.

Gunadi, A., Brandani, S., 2006. Diffusion of Linear Paraffins in NaCaA Studied by the ZLC Method. Microporous Mesoporous Mater. 90 (1), 278–283. https://doi.org/10.1016/j.micromeso.2005.11.027.

Hanikel, N., Prévot, M.S., Fathieh, F., Kapustin, E.A., Lyu, H., Wang, H., Diercks, N.J., Glover, T.G., Yaghi, O.M., 2019. Rapid Cycling and Exceptional Yield in a Metal-Organic Framework Water Harvester. ACS Cent. Sci. 5 (10), 1699–1706. https://doi.org/10.1021/acscentsci.9b00745.

Hanikel, N., Pei, X., Chheda, S., Lyu, H., Jeong, W., Sauer, J., Gagliardi, L., Yaghi, O.M., 2021. Evolution of Water Structures in Metal-Organic Frameworks for Improved Atmospheric Water Harvesting. Science 374 (6566), 454–459. https://doi.org/10.1126/science.abj0890.

Hossain, M.I., 2014. Volume Swing Frequency Response Method For Determining Mass Transfer Mechanisms in Microporous Adsorbents. Ph.D. Thesis, University of South Carolina, Columbia, South Carolina.

Hossain, M.I., Glover, T.G., 2019. Kinetics of Water Adsorption in UiO-66 MOF. Ind. Eng. Chem. Res. 58 (24), 10550–10558. https://doi.org/10.1021/acs.iecr.9b00976.

Hossain, M.I., Ebner, A.D., Ritter, J.A., 2016. New Linear Driving Force Correlation Spanning Long and Short Cycle Time Pressure Swing Adsorption Processes. Adsorption 22 (7), 939–950.

Hossain, M.I., Holland, C.E., Ebner, A.D., Ritter, J.A., 2019. 110th Anniversary: New Volumetric Frequency Response System for Determining Mass Transfer Mechanisms in Microporous Adsorbents. Ind. Eng. Chem. Res. 58 (37), 17462–17474. https://doi.org/10.1021/acs.iecr.9b02422.

Hossain, M.I., Holland, C.E., Ebner, A.D., Ritter, J.A., 2019. Mass Transfer Mechanisms and Rates of CO_2 and N_2 in 13X Zeolite from Volumetric Frequency Response. Ind. Eng. Chem. Res. 58 (47), 21679–21690. https://doi.org/10.1021/acs.iecr.9b04756.

Ji, J.G., Wang, R.Z., Li, L.X., 2007. New Composite Adsorbent for Solar-Driven Fresh Water Production from the Atmosphere. Desalination 212 (1), 176–182. https://doi.org/10.1016/j.desal.2006.10.008.

Jobic, H., Skoulidas, A.I., Sholl, D.S., 2004. Determination of Concentration Dependent Transport Diffusivity of CF4 in Silicalite by Neutron Scattering Experiments and Molecular Dynamics. J. Phys. Chem. B 108 (30), 10613–10616. https://doi.org/10.1021/jp048461k.

Kallenberger, P.A., Fröba, M., 2018. Water Harvesting from Air with a Hygroscopic Salt in a Hydrogel-Derived Matrix. Commun Chem 1 (1), 1–6. https://doi.org/10.1038/s42004-018-0028-9.

Kalmutzki, M.J., Diercks, C.S., Yaghi, O.M., 2018. Metal-Organic Frameworks for Water Harvesting from Air. Adv. Mater. 30 (37), 1704304. https://doi.org/10.1002/adma.201704304.

Kärger, J., 2015. Transport Phenomena in Nanoporous Materials. ChemPhysChem 16 (1), 24–51. https://doi.org/10.1002/cphc.201402340.

Kim, H., Yang, S., Rao, S.R., Narayanan, S., Kapustin, E.A., Furukawa, H., Umans, A.S., Yaghi, O.M., Wang, E.N., 2017. Water Harvesting from Air with Metal-Organic Frameworks Powered by Natural Sunlight. Science 356 (6336), 430–434. https://doi.org/10.1126/science.aam8743.

Kim, H., Rao, S.R., Kapustin, E.A., Zhao, L., Yang, S., Yaghi, O.M., Wang, E.N., 2018. Adsorption-Based Atmospheric Water Harvesting Device for Arid Climates. Nat. Commun. 9 (1), 1191. https://doi.org/10.1038/s41467-018-03162-7.

Klemm, O., Schemenauer, R.S., Lummerich, A., Cereceda, P., Marzol, V., Corell, D., van Heerden, J., Reinhard, D., Gherezghiher, T., Olivier, J., Osses, P., Sarsour, J., Frost, E., Estrela, M.J., Valiente, J.A., Fessehaye, G.M., 2012. Fog as a Fresh-Water Resource: Overview and Perspectives. AMBIO 41 (3), 221–234. https://doi.org/10.1007/s13280-012-0247-8.

Knox, J.C., Ebner, A.D., LeVan, M.D., Coker, R.F., Ritter, J.A., 2016. Limitations of Breakthrough Curve Analysis in Fixed-Bed Adsorption. Ind. Eng. Chem. Res. 55 (16), 4734–4748. https://doi.org/10.1021/acs.iecr.6b00516.

Kramers, H., Alberda, G., 1953. Frequency Response Analysis of Continuous Flow Systems. Chem. Eng. Sci. 2 (4), 173–181. https://doi.org/10.1016/0009-2509(53)80039-4.

LaPotin, A., Zhong, Y., Zhang, L., Zhao, L., Leroy, A., Kim, H., Rao, S.R., Wang, E.N., 2020. Dual-Stage Atmospheric Water Harvesting Device for Scalable Solar-Driven Water Production. Joule. https://doi.org/10.1016/j.joule.2020.09.008.

Laurenz, E., Füldner, G., Velte, A., Schnabel, L., Schmitz, G., 2021. Frequency Response Analysis for the Determination of Thermal Conductivity and Water Transport in MOF Adsorbent Coatings for Heat Transformation. Int. J. Heat Mass Transf. 169, 120921 https://doi.org/10.1016/j.ijheatmasstransfer.2021.120921.

LeVan, M.D., Carta, G., 2008. Section 16: adsorption and ion exchange. In. In: Green, D. W., Maloney, J.O. (Eds.), Perry's Chemical Engineers'Handbook, 8th ed. McGraw-Hill, NewYork.

Li, R., Shi, Y., Alsaedi, M., Wu, M., Shi, L., Wang, P., 2018. Hybrid Hydrogel with High Water Vapor Harvesting Capacity for Deployable Solar-Driven Atmospheric Water Generator. Environ. Sci. Technol. 52 (19), 11367–11377. https://doi.org/10.1021/acs.est.8b02852.

Li, R., Shi, Y., Shi, L., Alsaedi, M., Wang, P., 2018. Harvesting Water from Air: Using Anhydrous Salt with Sunlight. Environ. Sci. Technol. 52 (9), 5398–5406. https://doi.org/10.1021/acs.est.7b06373.

Li, R., Shi, Y., Wu, M., Hong, S., Wang, P., 2020. Improving Atmospheric Water Production Yield: Enabling Multiple Water Harvesting Cycles with Nano Sorbent. Nano Energy 67, 104255. https://doi.org/10.1016/j.nanoen.2019.104255.

Li, Y.-E., Willcox, D., Gonzalez, R.D., 1989. Determination of Rate Constants by the Frequency Response Method: CO on Pt/SiO2. AIChE J. 35 (3), 423–428. https://doi.org/10.1002/aic.690350310.

Liu, J., Wang, Y., Benin, A.I., Jakubczak, P., Willis, R.R., LeVan, M.D., 2010. CO_2 /H_2O Adsorption Equilibrium and Rates on Metal−Organic Frameworks: HKUST-1 and Ni/DOBDC. Langmuir 26 (17), 14301–14307. https://doi.org/10.1021/la102359q.

Logan, M.W., Langevin, S., Xia, Z., 2020. Reversible Atmospheric Water Harvesting Using Metal-Organic Frameworks. Sci. Rep. 10 (1), 1492. https://doi.org/10.1038/s41598-020-58405-9.

Macedonio, F., Drioli, E., Gusev, A.A., Bardow, A., Semiat, R., Kurihara, M., 2012. Efficient Technologies for Worldwide Clean Water Supply. Chem. Eng. Process. Process Intensif. 51, 2–17. https://doi.org/10.1016/j.cep.2011.09.011.

Nemiwal, M., Kumar, D., 2020. Metal Organic Frameworks as Water Harvester from Air: Hydrolytic Stability and Adsorption Isotherms. Inorg. Chem. Commun. 122, 108279 https://doi.org/10.1016/j.inoche.2020.108279.

O'Brien, M. J.; Moore, D. R.; Alberts, W. C.; Yang, J.; Doherty, M. D.; Buckley, M. D.; Howson, J. E.; Lipinski, B. M. "System and Method for Fluid Capture using a Cross-linked Binder", US Patent Applications (17/932,158), 2022.

Onyestyák, G., Rees, L.V.C., 1999. Frequency Response Study of Adsorbate Mobilities of Different Character in Various Commercial Adsorbents. J. Phys. Chem. B 103 (35), 7469–7479. https://doi.org/10.1021/jp990662e.

Onyestyák, G., Shen, D., Rees, L.V.C., 1995. Frequency-Response Study of Micro- and Macro-Pore Diffusion in Manufactured Zeolite Pellets. J Chem Soc Faraday Trans 91 (9), 1399–1405. https://doi.org/10.1039/FT9959101399.

Onyestyák, G., Shen, D., Rees, L.V.C., 1996. Frequency-Response Studies of CO2 Diffusion in Commercial 5A Powders and Pellets. Microporous Mater. 5 (5), 279–288. https://doi.org/10.1016/0927-6513(95)00062-3.

Park, I.S., Petkovska, M., Do, D.D., 1998. Frequency Response of an Adsorber with Modulation of the Inlet Molar Flow-Rate—I. A Semi-Batch Adsorber. *Chem. Eng. Sci.* 53 (4), 819–832. https://doi.org/10.1016/S0009-2509(97)00371-0.

Park, I.S., Petkovska, M., Do, D.D., 1998. Frequency Response of an Adsorber with Modulation of the Inlet Molar Flow-Rate—II. A Continuous Flow Adsorber. Chem. Eng. Sci. 53 (4), 833–843. https://doi.org/10.1016/S0009-2509(97)00372-2.

Peeters, R., Vanderschaeghe, H., Rongé, J., Martens, J.A., 2020. Energy Performance and Climate Dependency of Technologies for Fresh Water Production from Atmospheric Water Vapour. Environ. Sci. Water Res. Technol. 6 (8), 2016–2034. https://doi.org/10.1039/D0EW00128G.

Rajniak, P., Yang, R.T., 1993. A Simple Model and Experiments for Adsorption-Desorption Hysteresis: Water Vapor on Silica Gel. AIChE Journal 39 (5), 774–786. https://doi.org/10.1002/aic.690390506.

Rieth, A.J., Wright, A.M., Skorupskii, G., Mancuso, J.L., Hendon, C.H., Dincă, M., 2019. Record-Setting Sorbents for Reversible Water Uptake by Systematic Anion Exchanges in Metal-Organic Frameworks. J. Am. Chem. Soc. 141 (35), 13858–13866. https://doi.org/10.1021/jacs.9b06246.

Roque-Malherbe, R.M., 2007. *Adsorption and diffusion in nanoporous materials*. CRC press.

Rossin, J., Petersen, E., Tevault, D., Lamontagne, R., Isaacson, L., 1991. Effects of Environmental Weathering on the Properties of ASC-Whetlerite. Carbon 29 (2), 197–205. https://doi.org/10.1016/0008-6223(91)90070-Y.

Rudisill, E.N., Hacskaylo, J.J., LeVan, M.D., 1992. Coadsorption of Hydrocarbons and Water on BPL Activated Carbon. Ind. Eng. Chem. Res. 31 (4), 1122–1130. https://doi.org/10.1021/ie00004a022.

Ruthven, D.M., 1984. Principles of Adsorption and Adsorption Processes. John Wiley & Sons.

Ruthven, D.M., 2004. Sorption Kinetics for Diffusion-Controlled Systems with a Strongly Concentration-Dependent Diffusivity. Chem. Eng. Sci. 59 (21), 4531–4545.

Ruthven, D.M., Brandani, S., Eic, M., 2008. Measurement of Diffusion in Microporous Solids by Macroscopic Methods. In: Karge, H.G., Weitkamp, J. (Eds.), Mol. Sieves - Sci. Technol. 7, 45–84.

Ruthven, D.M., Lee, L.-K., 1981. Kinetics of Nonisothermal Sorption: Systems with Bed Diffusion Control. AIChE Journal 27 (4), 654–663. https://doi.org/10.1002/aic.690270418.

Ruthven, D.M., Lee, L.-K., Yucel, H., 1980. Kinetics of Non-Isothermal Sorption in Molecular Sieve Crystals. AIChE Journal 26 (1), 16–23. https://doi.org/10.1002/aic.690260104.

Sartory, W.K., 1978. Adsorption on the Walls of a Cylindrical Channel. Ind. Eng. Chem. Fund. 17 (2), 97–101. https://doi.org/10.1021/i160066a005.

Sharp, H., C., C. Bukowski, B., Li, H., M. Johnson, E., Ilic, S., J. Morris, A., Gersappe, D., Q. Snurr, R., R. Morris, J., 2021. Nanoconfinement and Mass Transport in Metal-Organic Frameworks. Chem. Soc. Rev. https://doi.org/10.1039/D1CS00558H.

Silva, JoséA, C., Rodrigues, A. E., 1996. Analysis of ZLC Technique for Diffusivity Measurements in Bidisperse Porous Adsorbent Pellets. Gas Sep. Purif. 10 (4), 207–224. https://doi.org/10.1016/S0950-4214(96)00021-7.

Skoulidas, A.I., Sholl, D.S., 2005. Self-Diffusion and Transport Diffusion of Light Gases in Metal-Organic Framework Materials Assessed Using Molecular Dynamics Simulations. J. Phys. Chem. B 109 (33), 15760–15768. https://doi.org/10.1021/jp051771y.

Sleiti, A.K., Al-Khawaja, H., Al-Khawaja, H., Al-Ali, M., 2021. Harvesting Water from Air Using Adsorption Material – Prototype and Experimental Results. Sep. Purif. Technol. 257, 117921 https://doi.org/10.1016/j.seppur.2020.117921.

Song, L.; Rees, L. V. C. Frequency Response Measurements of Diffusion in Microporous Materials. In *Adsorption and Diffusion*; Karge, H. G., Weitkamp, J., Eds.; Molecular Sieves; Springer: Berlin, Heidelberg, 2008; pp 235–276. https://doi.org/10.1007/3829_2007_013.

Song, L., Rees, L.V.C., 1997. Adsorption and Transport of N-Hexane in Silicalite-1 by the Frequency Response Technique. J. Chem. Soc. Faraday Trans. 93 (4), 649–657. https://doi.org/10.1039/a606468j.

Song, L., Rees, L.V.C., 2000. Adsorption and Diffusion of Cyclic Hydrocarbon in MFI-Type Zeolites Studied by Gravimetric and Frequency-Response Techniques. Microporous Mesoporous Mater. 35–36, 301–314. https://doi.org/10.1016/S1387-1811(99)00229-2.

Sward, B.K., LeVan, M.D., 2003. Frequency Response Method for Measuring Mass Transfer Rates in Adsorbents via Pressure Perturbation. Adsorption 9 (1), 37–54. https://doi.org/10.1023/A:1023863213893.

Tereck, C.D., Kovach, D.S., LeVan, M.D., 1987. Constant-Pattern Behavior for Adsorption on the Wall of a Cylindrical Channel. Ind. Eng. Chem. Res. 26 (6), 1222–1227. https://doi.org/10.1021/ie00066a027.

Tovar, T.M., Zhao, J., Nunn, W.T., Barton, H.F., Peterson, G.W., Parsons, G.N., LeVan, M. D., 2016. Diffusion of CO_2 in Large Crystals of Cu-BTC MOF. J. Am. Chem. Soc. 138 (36), 11449–11452. https://doi.org/10.1021/jacs.6b05930.

Towsif Abtab, S.M., Alezi, D., Bhatt, P.M., Shkurenko, A., Belmabkhout, Y., Aggarwal, H., Weseliński, Ł.J., Alsadun, N., Samin, U., Hedhili, M.N., Eddaoudi, M., 2018. Reticular Chemistry in Action: A Hydrolytically Stable MOF Capturing Twice Its Weight in Adsorbed Water. Chem 4 (1), 94–105. https://doi.org/10.1016/j.chempr.2017.11.005.

Tu, Y., Wang, R., Zhang, Y., Wang, J., 2018. Progress and Expectation of Atmospheric Water Harvesting. Joule 2 (8), 1452–1475. https://doi.org/10.1016/j.joule.2018.07.015.

Valyon, J., Onyestyák, G.y., Rees, L.V.C., 2000. A Frequency-Response Study of the Diffusion and Sorption Dynamics of Ammonia in Zeolites. Langmuir 16 (3), 1331–1336. https://doi.org/10.1021/la990867e.

Wang, Y., 2021. Identification of Mass Transfer Resistances in Microporous Materials Using Frequency Response Methods. Adsorption. https://doi.org/10.1007/s10450-021-00305-z.

Wang, Y., LeVan, M.D., 2005. Investigation of Mixture Diffusion in Nanoporous Adsorbents via the Pressure-Swing Frequency Response Method. 2. Oxygen and Nitrogen in a Carbon Molecular Sieve. Ind. Eng. Chem. Res. 44 (13), 4745–4752. https://doi.org/10.1021/ie0489352.

Wang, Y., LeVan, M.D., 2005. Investigation of Mixture Diffusion in Nanoporous Adsorbents via the Pressure-Swing Frequency Response Method. 1. Theoretical Treatment. Ind. Eng. Chem. Res. 44 (10), 3692–3701. https://doi.org/10.1021/ie048936u.

Wang, Y., LeVan, M.D., 2007. Mixture Diffusion in Nanoporous Adsorbents: Development of Fickian Flux Relationship and Concentration-Swing Frequency Response Method. Ind. Eng. Chem. Res. 46 (7), 2141–2154. https://doi.org/10.1021/ie061214d.

Wang, Y., LeVan, M.D., 2008. Nanopore Diffusion Rates for Adsorption Determined by Pressure-Swing and Concentration-Swing Frequency Response and Comparison with Darken's Equation. Ind. Eng. Chem. Res. 47 (9), 3121–3128. https://doi.org/10.1021/ie070673r.

Wang, Y., LeVan, M.D., 2011. Master Curves for Mass Transfer in Bidisperse Adsorbents for Pressure-Swing and Volume-Swing Frequency Response Methods. AIChE J. 57 (8), 2054–2069. https://doi.org/10.1002/aic.12420.

Wang, X., Li, X., Liu, G., Li, J., Hu, X., Xu, N., Zhao, W., Zhu, B., Zhu, J., 2019. An Interfacial Solar Heating Assisted Liquid Sorbent Atmospheric Water Generator. Angew. Chem. Int. Ed. 58 (35), 12054–12058. https://doi.org/10.1002/anie.201905229.

Wang, J.-Y., Mangano, E., Brandani, S., Ruthven, D.M., 2021. A Review of Common Practices in Gravimetric and Volumetric Adsorption Kinetic Experiments. Adsorption 27 (3), 295–318. https://doi.org/10.1007/s10450-020-00276-7.

Wang, Y., Sward, B.K., LeVan, M.D., 2003. New Frequency Response Method for Measuring Adsorption Rates via Pressure Modulation: Application to Oxygen and Nitrogen in a Carbon Molecular Sieve. Ind. Eng. Chem. Res. 42 (18), 4213–4222. https://doi.org/10.1021/ie030206j.

Wang, Y., Mahle, J.J., Furtado, A.M.B., Glover, T.G., Buchanan, J.H., Peterson, G.W., LeVan, M.D., 2013. Mass Transfer and Adsorption Equilibrium for Low Volatility Alkanes in BPL Activated Carbon. Langmuir 29 (9), 2935–2945. https://doi.org/10.1021/la304926x.

Xu, J., Li, T., Chao, J., Wu, S., Yan, T., Li, W., Cao, B., Wang, R., 2020. Efficient Solar-Driven Water Harvesting from Arid Air with Metal-Organic Frameworks Modified by Hygroscopic Salt. Angew. Chem. Int. Ed. 59 (13), 5202–5210. https://doi.org/10.1002/anie.201915170.

Xu, W., Yaghi, O.M., 2020. Metal-Organic Frameworks for Water Harvesting from Air, Anywhere. Anytime. *ACS Cent. Sci.* 6 (8), 1348–1354. https://doi.org/10.1021/acscentsci.0c00678.

Yaghi, O.M., Kalmutzki, M.J., Diercks, C.S., 2019. Introduction to Reticular Chemistry: Metal-Organic Frameworks and Covalent Organic Frameworks. John Wiley & Sons.

Tovar, T. M., 2016. Adsorption Equilibria and Mass Transfer in Porous Adsorbents. Ph.D. Thesis, Vanderbilt University, Nashville, Tennessee.

Yang, K.; Pan, T.; Lei, Q.; Dong, X.; Cheng, Q.; Han, Y. A Roadmap to Sorption-Based Atmospheric Water Harvesting: From Molecular Sorption Mechanism to Sorbent Design and System Optimization. *Environ. Sci. Technol.* **2021**, acs.est.1c00257. https://doi.org/10.1021/acs.est.1c00257.

Yang, K., Shi, Y., Wu, M., Wang, W., Jin, Y., Li, R., Shahzad, M.W., Ng, K.C., Wang, P., 2020. Hollow Spherical SiO2 Micro-Container Encapsulation of LiCl for High-Performance Simultaneous Heat Reallocation and Seawater Desalination. J. Mater. Chem. A 8 (4), 1887–1895. https://doi.org/10.1039/C9TA11721K.

Yasuda, Y., 1976. Frequency Response Method for Study of the Kinetic Behavior of a Gas-Surface System. 1. Theoretical Treatment. J. Phys. Chem. 80 (17), 1867–1869. https://doi.org/10.1021/j100558a010.

Yasuda, Y., 1982. Determination of Vapor Diffusion Coefficients in Zeolite by the Frequency Response Method. J. Phys. Chem. 86 (10), 1913–1917. https://doi.org/10.1021/j100207a036.

Yasuda, Y., 1993. Frequency Response Method for Study of Kinetic Details of a Heterogeneous Catalytic Reaction of Gases. 1. Theoretical Treatment. J. Phys. Chem. 97 (13), 3314–3318. https://doi.org/10.1021/j100115a036.

Yasuda, Y., Matsumoto, K., 1989. Straight- and Cross-Term Diffusion Coefficients of a Two-Component Mixture in Micropores of Zeolites by Frequency Response Method. J. Phys. Chem. 93 (8), 3195–3200. https://doi.org/10.1021/j100345a062.

Zhou, X., Lu, H., Zhao, F., Yu, G., 2020. Atmospheric Water Harvesting: A Review of Material and Structural Designs. ACS Mater. Lett. 2 (7), 671–684. https://doi.org/10.1021/acsmaterialslett.0c00130.